Original Paper

Origin of facies-controlled dolomite and exploration significance of the Middle Permian Qixia Formation in central Sichuan Basin, Western China

Xiao-Liang Bai [a], Long Wen [a], Yong-Mei Zhang [b, c, *], Xi-Hua Zhang [a], Jing Wang [a], Yan-Gui Chen [a], Si-Qiao Peng [a], Wei Wang [a], Jia-Yi Zhong [a], Ya Li [a], Ping Gao [d]

[a] Research Institute of Exploration and Development, PetroChina Southwest Oil and Gas Field Company, Chengdu, 610051, Sichuan, China
[b] State Key Laboratory of Oil and Gas Reservoir Geology and Exploitation, Chengdu University of Technology, Chengdu, 610059, Sichuan, China
[c] College of Energy (College of Modern Shale Gas Industry), Chengdu University of Technology, Chengdu, 610059, Sichuan, China
[d] Exploration Division, PetroChina Southwest Oil and Gas Field Company, Chengdu, 610051, Sichuan, China

ARTICLE INFO

ABSTRACT

The intraplatform shoal dolomite of the Middle Permian Qixia Formation is currently considered the key target of hydrocarbon exploration in the central Sichuan Basin. To systematically investigate the origin of the stratabound facies-controlled porous dolomites of the Qixia Formation, integrated petrography, logging and seismic analysis were carried out in this work. The results are as following: (1) the dolomite reservoir is universal in the central Sichuan Basin, and its distribution is controlled by intraplatform shoals, with multilayer superposition vertically. Thick massive dolostone may also develop along with the fault. (2) Three replaced dolomites and one dolomite cement were identified: very finely to finely crystalline, anhedral to subhedral dolomite (Rd1); finely to medium crystalline, anhedral to subhedral dolomite (Rd2); coarsely crystalline, subhedral to euhedral dolomite (Rd3) and coarsely crystalline saddle dolomite cement (Sd). Rd2 and Rd3 are partly fabric-retentive, and preserve the original bioclastic ghosts. Sd shows wavy extinction, filled in the breccia veins. (3) The U-Pb dating and homogenization temperatures results indicate that the dolomite and Sd cement are associated with hydrothermal event during the Emeishan large igneous province. The δ^{13}C, ^{87}Sr/^{86}Sr, and seawater-like REEY patterns suggest that the dolomitization and Sd precipitation fluids originate from connate seawater heated by elevated heat-flow. (4) The ELIP triggered large scale thermal anomalies in the basin during the Dongwu movement period. The increased temperature and pressure drove the formation water in the intra-platform shoal facies and overcame the binding effect of Mg^{2+} hydrate. Moreover, the deep hydrothermal fluid preferentially penetrated into the porous strata of shoal facies along the faults and fractures, mixed with formation water to some extent, and extensive dolomitization occurred. The facies-controlled dolomite reservoir and the underlying Cambrian source rock form a good source-reservoir assemblage, which can be a key replacement option.

1. Introduction

It has been reported that more than 50 % of worldwide carbonate reservoirs are dolomite (Machel, 2004). Therefore, hydrocarbon exploration of dolomite reservoirs is particularly important. A variety of theories and geological models have been proposed in the literature for the genetic interpretation of dolomite, such as the Neoproterozoic "dolomite sea" hypothesis (Wang et al., 2020; Jiang et al., 2022), seepage-reflux (Adams and Rhodes, 1960; Shields and Brady, 1995; Jones et al., 2003; Jiang et al., 2014), Sabkha (Illing and Wells, 1965), evaporation pump (Hsu and Siegenth, 1969), mixed water (Badiozamani, 1973), burial (Zenger, 1983; Machel and Anderson, 1989), seawater (Land, 1985),

* Corresponding author. State Key Laboratory of Oil and Gas Reservoir Geology and Exploitation, Chengdu University of Technology, Chengdu, 610059, Sichuan, China.
E-mail address: 1605058851@qq.com (Y.-M. Zhang).

hydrothermal (Fanning et al., 1981; Davies and Smith, 2006; Hollis et al., 2017) and microbial dolomitization models (Vasconcelos and Mckenzie, 1997). In the previous works, the time and genetic model of dolomitization have been carefully examined based on dolomite distribution characteristics, the sources of dolomitization fluids and fluid circulation (Warren, 2000; Machel, 2004). Many scholars have studied on hydrothermal and hydrothermally-altered dolostones (Davies and Smith, 2006; Hollis et al., 2017; Koeshidayatullah et al., 2020; Pan et al., 2020). The hydrothermal dolomites are widely distributed near faults, and most are massive and breccia-shaped rather than layered. They show a bottom-up, non-fabric-selective replacing diagenetic sequence along extensional strike-slip faults. The deeply burial brines and seawaters may be driven by the thermal anomaly, resulting in the massive dolomitization (Consonni et al., 2018; Hollis et al., 2017; Hirani et al., 2018). Those sources of dolomitization fluids and the characteristics of hydrological fluid circulation explain the mechanism of dolostones within a particular model. However, the fluid sources, distribution and hydrological mechanism of hydrothermal dolomitization in facies-controlled dolostones in different diagenetic stages have not been reported.

In recent years, dolomite reservoirs of the Middle Permian Qixia Formation have shown considerable hydrocarbon potential in the Sichuan Basin, western China. High yields of commercial natural gas flow of several exploratory wells from the Qixia Formation have further confirmed the existence of large-scale, porous dolomite reservoirs in the platform margin belt of the western Sichuan Basin. Also, many wells have been drilled into cyclic, thin-layered, continuous and porous dolomite reservoirs, showing the existence of intraplatform shoal dolomite gas reservoirs in the central Sichuan Basin. For instance, wells MX42 and MX31X1 produce up to 46×10^4 and 70×10^4 cubic meters of natural gas per day (m^3/d), respectively. Therefore, the thin-layered porous dolomite reservoirs of the Qixia Formation are a major target of exploration in the central Sichuan Basin (Fig. 1). The dolomitization mechanisms of the Middle Permian Qixia Formation carbonates in Sichuan Basin have been discussed in detail and refined by a series of studies. They include mixed water dolomitization (Chen, 1989), burial dolomitization (Jiang et al., 2009), hydrothermal dolomitization (Huang et al., 2012, 2014; Li et al., 2016; Jiang et al., 2016; Pan et al., 2021), and penecontemporaneous seawater dolomitization (Jiang et al., 2016; Li et al., 2020; Lu et al., 2020). Also, some scholars proposed that the dolomitization resulted from meteoric water leaching the Emeishan basalt which provided abundant Mg^{2+} (Jin and Feng, 1999). However, most of those studies have not provided comprehensive stratigraphy, petrography and/or geochemical frameworks. Furthermore, the facies-controlled dolostone of the Qixia Formation is characterized by thin layers, multilayers superpositioned vertically, and strong lateral heterogeneity, which challenge the traditional dolomitization mechanism.

To effectively address these issues, in this work, the thin-layered, facies-controlled, and porous dolomite of the Qixia Formation was investigated based on core and thin section observations, cathodoluminescence, well-logging, isotopic geochemistry and fluid inclusion microthermometry. The goals were to: (1) further clarify the dolomite distribution and dolomitization mechanism; and (2) provide support and reference for subsequent hydrocarbon exploration and evaluation of the Qixia Formation.

2. Geological setting

The central Sichuan Basin lies between the Longquanshan-Santai-Bazhong-Zhenba fault zone and the Huayingshan fault zone (Hu and Xie, 1997). The basement comprises the lower crystalline basement and the Kangding Group and older

basic—ultrabasic rocks, without an upper fold basement. Such types of differences in the formation and evolution of the basement gave rise to two groups of basement faults (NE and NW), which generally comprise a rhombic fault system. The basement faults were active in multiple periods. Strike-slip extensional or strike-slip deep faults have been developed in the Caledonian to Hercynian orogenies, and they determined the stratigraphic thicknesses and the variations in sedimentary facies to a certain extent. Such deep faults have been transformed from early normal faults to late reverse faults in the Indosinian to Himalayan orogenies (Yin et al., 2013). The tectonic movement at the end of the Caledonian orogeny caused the uplifting of the central Sichuan Basin, which gradually shaped the Leshan-Longnüsi paleo-uplift (Xu et al., 2012; Li et al., 2014). In addition, the Sinian, Cambrian, Ordovician and Silurian strata have suffered from various degrees of denudation by drilling and cores in the outer circumference of the paleo-uplift. In the Hercynian, most of the Yangtze platform continued to rise to become land, and the periphery (the Longmenshan piedmont) was sharply rifted. Clastic rock deposition transitioned to carbonate deposition during in the Devonian to Carboniferous, which had a hiatus in the central Sichuan Basin (Chen et al., 2011). That tectonic pattern lasted until the Permian, and stable carbonate platform deposits were developed in the central Sichuan Basin from the Permian to the Middle Triassic (Chen et al., 2011). Along with the Indosinian Movement at the end of the Middle Triassic, the Longmenshan piedmont was uplifted to provide substantial materials. The carbonate sedimentary system transitioned into a clastic rock sedimentary system, and the basin received extensive deposits during the Upper Triassic, Jurassic, and Cretaceous (Shi, 2001; Chen et al., 2004; He et al., 2011).

In the Middle Permian, the glaciers in the Gondwana continent melted in the interglacial period, and the global sea level (especially in South China) continued to rise (Huang et al., 2014). Gradually, the seawater transgressed from the periphery to the paleo-uplift, and the strata overlapped the central-western Sichuan paleo-uplift. The carbonate platform deposits were developed in the Qixia-Maokou formations. Controlled by the pre-Permian paleogeomorphology and the peripheral rift basins, in the western Sichuan Basin, carbonate platform margin deposits and thick-layer grain shoal dolomite were developed. In the central Sichuan Basin, at the slope break of the paleo-uplift, the Qixia Formation has deposited alternately with intraplatform shoal and intershoal subfacies, consisting of sparite grainstone and micrite interbeds lithologically (Fig. 2). The Qixia Formation with a thickness of 105—125 m thick, is a sedimentary sequence longitudinally comprising a set of grey black to dark grey chert nodule and bioclast-bearing micrite limestone, with deepwater biological assemblages of planktonic foraminifera, coccolith and calcium spheres. In the Middle-Lower part, interbed dolomite and calcareous dolomite with grain residues are developed by replacing grey lime-packstone and lime-grainstone.

During the Maokou Formation period, extensional tectonic activities tended to be frequent, and tectonic sedimentary differentiation occurred, with the development of intracraton rifted trough basins striking NWW and NE. Sedimentary differentiation occurred on the platform (Chen et al., 1999), showing great differences in sedimentary thickness. In the central Sichuan Basin, the Maokou Formation is 190—315 m thick totally, and composed mainly of grey bioclastic limestone, light grey bioclastic limestone, and dark grey argillaceous limestone intercalated with black shale. In the early to middle Maokou Formation, the extensional activity intensified, and a large set of siliceous and magnesial hydrothermal minerals was deposited under the control of extensional and strike-slip faults (Fig. 2). At the end of the Middle Permian period, the Emei taphrogeny during the Dongwu Movement resulted in large-scale basalt magma eruptions. Thick layers of eruptive basalt emerged in the
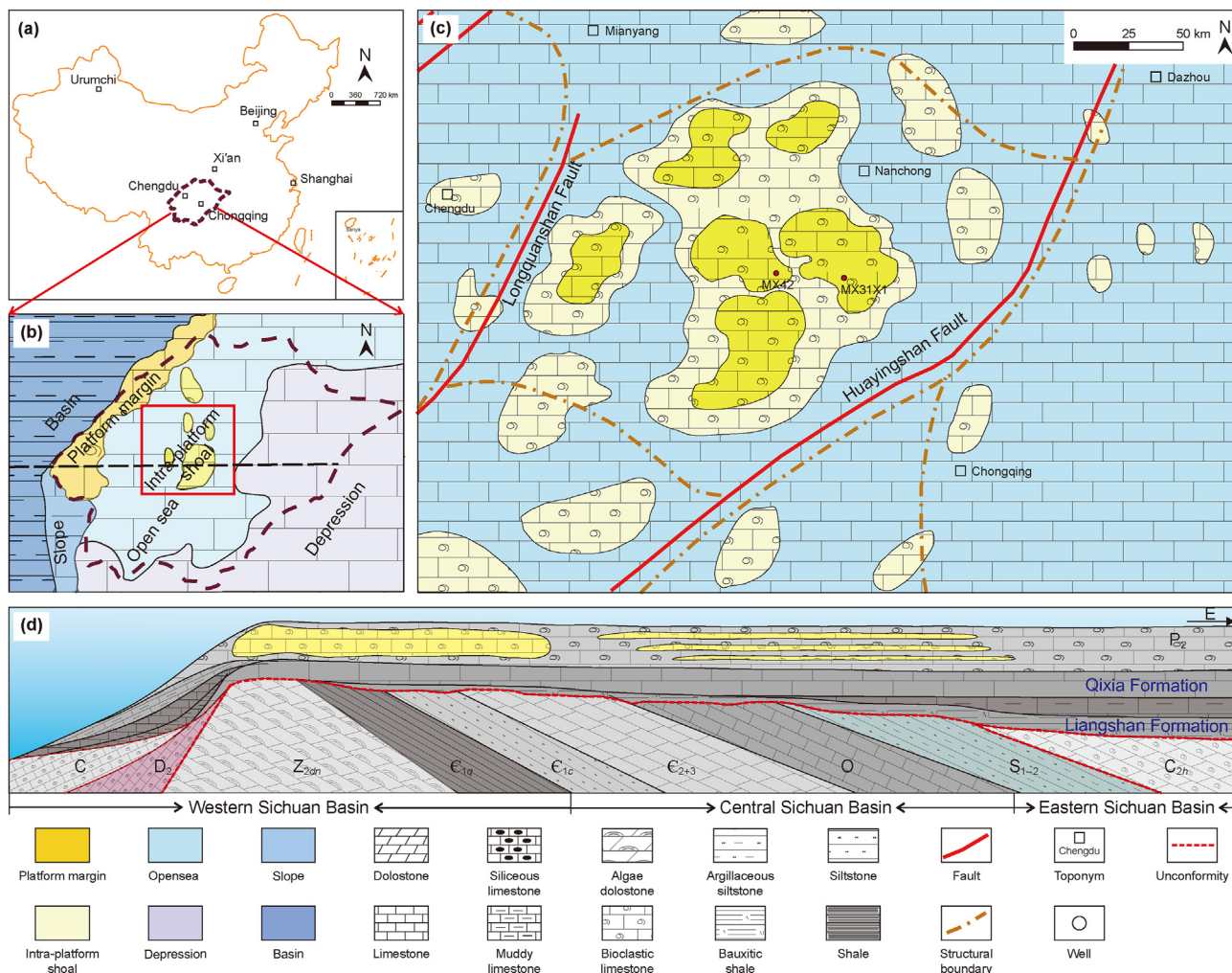
Fig. 1. (a) Location of the Sichuan Basin in China. **(b)** Detailed map of the study area and the related stratigraphic distribution, locations of wells and dolomite distribution. **(c)** Palaeogeographic map reconstruction of the Sichuan Basin during the Middle Permian. **(d)** Stratigraphic section of the Sichuan Basin showing the marine sedimentary characteristics and stratigraphic contacts from the Sinian to Permian periods.

central−southwestern Sichuan Basin, forming a hiatus between the Late Permian and the Middle Permian (Yin et al., 2018; Shi and Grunt, 2000).

3. Methods

To understand the origin of the Qixia Formation dolomites and dolomite cement in the central Sichuan Basin, the samples were selected for carbon and oxygen isotopes, strontium isotope, inclusion homogenization temperature, and last ice-melting temperature. In this study, 165 cores of the Qixia Formation dolomite were taken from the coring wells of MX108, MX42, MX150, and MX117 (Table 1). All cores, without signs of weathering and denudation, were subjected to thin section identification (being stained by alizarin red and potassium ferricyanide) and cathodoluminescence analysis. 35 dolomite and 26 limestone samples were preferentially prepared and finely selected for geochemical analysis.

The analysis of carbon, oxygen and strontium isotopes was completed in the Isotope Analysis Room PetroChina Hangzhou Institute of Geology. The MAT252 gas isotope mass spectrometer and 100 % phosphoric acid solution were used for the carbon and oxygen isotope analysis, with an error of 0.01 % in contrast to the GBW04406 standard sample. For the strontium isotope analysis,

approximately 70 mg core sample was crushed to 200 mesh, and dissolved in a Teflon cup with 0.8 mol/L hydrochloric acid for 2 h. After centrifugation, the solution was passed through an AG50W × 8(H$^+$) cation exchange column, and with hydrochloric acid as the eluent, pure strontium was extracted. Finally, strontium isotope was measured on a VG354 solid isotope mass spectrometer. The blank background of the entire process was about 2×10^{-10} to 5×10^{-10} g, with the error expressed as 2σ ($\pm$). The carbon, oxygen and strontium isotopes of dolomite and limestone are shown in Table 1 (details in Section 5.1).

In situ trace elemental tests were conducted at the Laboratory of Sichuan Chuangyuan Weipu Analytical Technology Company, China. The laser-spot size and frequency in this study were set to 120 μm and 5 Hz, respectively. Raw REEY concentrations (rare earth elements and yttrium) were normalized to Post-Archean Australian Shale (PAAS) (McLennan, 1989). The relative enrichments of the LREE (from La to Nd) and MREE (from Sm to Dy) were evaluated by the ratios of $(Pr/Yb)_{SN}$ and $(Pr/Tb)_{SN}$, respectively. The BSI (MREE enrichment) value was calculated following Tostevin et al. (2016). Ce and Pr anomalies were $(Ce/Ce^*)_{SN} = 2Ce_{SN}/(La_{SN} + Pr_{SN})$, and $(Pr/Pr^*)_{SN} = 2Pr_{SN}/(Ce_{SN} + Nd_{SN})$, respectively (the subscripted SN means PAAS-normalized) (Lawrence et al., 2006) (Table 2).

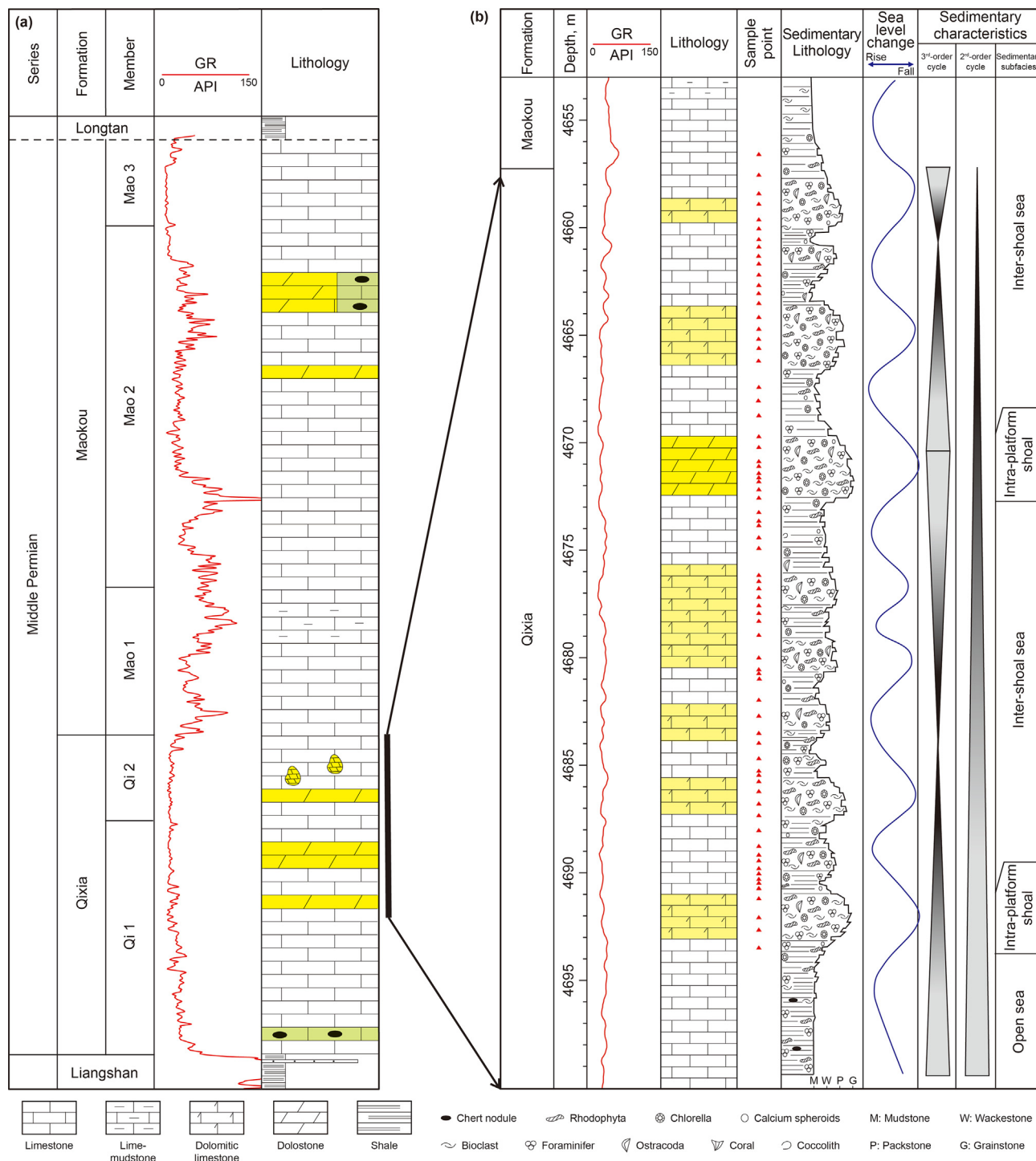Liquid-dominated aqueous inclusions in finely to medium

Fig. 2. (a) Schematic diagram of the stratigraphy in the Sichuan Basin. **(b)** Lithologic column of the Qixia Formation in the study area (Well MX108).

crystalline anhedral to subhedral dolomite (Rd2), coarsely crystalline dolomite (Rd3) and saddle dolomite cement (Sd) were measured for homogenization temperature (87 samples) and freezing point temperature (31 samples) (Table 3). The salinity of diagenetic fluid was estimated according to the NaCl equivalent solution salinity conversion formula provided by Bodnar (1993). The inclusion temperature was measured at the Institute of Geology of the Ministry of Nuclear Industry, using the LINKAMTHM S600 hot and cold machine. Inclusion temperatures of Rd2, Rd3 and

Sd were measure subject to the determination for Fluid Inclusion in Minerals (EJ/T1105-1999). The results are listed in Table 3.

LA-ICP-MS in situ U-Pb dating of Rd3 and Sd were performed at the Laboratory of Sichuan Chuangyuan Weipu Analytical Technology Company, China. The dolomite samples were made into standard 2.5 cm diameter mounts and polished. The mounts were thoroughly cleaned with MilliQ water in a sonicator, and dried overnight at 45−60 °C on a hot plate. Carbonate U-Pb dating was conducted using a Thermo Scientific quatraple iCap TQ inductively

Table 1
Isotopic compositions of the Qixia Formation carbonate in the central Sichuan Basin.

Well	Depth, m	Lithology	$\delta^{18}O$ (‰, VPDB)	$\delta^{13}C$ (‰, VPDB)	$^{87}Sr/^{86}Sr$ (±standard error)
MX108	4673.28	Micrite limestone	−6.81	3.43	$0.70822 \pm 6 \times 10^{-6}$
MX108	4662.55	Micrite limestone	−6.55	4.52	$0.70772 \pm 4 \times 10^{-6}$
MX108	4666.15	Micrite limestone	−7.23	4.36	
MX108	4657.13	Micrite limestone	−5.85	3.52	$0.70820 \pm 5 \times 10^{-6}$
MX108	4674.25	Micrite limestone	−6.73	4.64	$0.70800 \pm 4 \times 10^{-6}$
MX108	4681.00	Micrite limestone	−6.64	4.20	$0.70741 \pm 3 \times 10^{-6}$
MX108	4663.08	Micrite limestone	−7.28	4.86	
MX108	4680.33	Micrite limestone	−5.47	3.71	
MX108	4674.68	Micrite limestone	−6.76	4.57	
MX108	4661.86	Micrite limestone	−7.17	4.75	
MX108	4668.20	Micrite limestone	−7.01	5.02	$0.70781 \pm 4 \times 10^{-6}$
MX108	4678.30	Micrite limestone	−7.10	4.45	
MX108	4665.05	Micrite limestone	−7.28	3.78	$0.70777 \pm 4 \times 10^{-6}$
MX42	4659.63	Micrite limestone	−7.09	3.26	
MX108	4685.2	Micrite limestone	−4.67	4.43	
MX108	4672.99	Micrite limestone	−7.48	3.66	
MX108	4677.70	Micrite limestone	−6.29	2.42	$0.70729 \pm 4 \times 10^{-6}$
MX150	4490.64	Micrite limestone	−5.38	3.20	$0.70728 \pm 3 \times 10^{-6}$
MX150	4496.38	Micrite limestone	−5.64	3.25	$0.70733 \pm 4 \times 10^{-6}$
MX150	4498.73	Micrite limestone	−6.37	3.10	
MX150	4500.41	Micrite limestone	−5.89	3.5	
MX117	4603.31	Micrite limestone	−5.65	4.12	$0.70715 \pm 4 \times 10^{-6}$
MX117	4610.26	Micrite limestone	−6.35	3.52	$0.70724 \pm 5 \times 10^{-6}$
MX117	4613.78	Micrite limestone	−5.87	3.26	
MX42	4650.5	Micrite limestone	−6.95	3.21	$0.70703 \pm 4 \times 10^{-6}$
MX42	4655.8	Micrite limestone	−6.84	3.32	$0.70745 \pm 5 \times 10^{-6}$
MX42	4652.0	Rd2	−8.12	5.05	$0.70806 \pm 5 \times 10^{-6}$
MX42	4655.52	Rd2	−8.34	4.87	$0.70822 \pm 5 \times 10^{-6}$
MX42	4653.48	Rd2	−8.34	3.70	$0.70822 \pm 4 \times 10^{-6}$
MX42	4691.0	Rd2	−8.36	3.90	$0.70815 \pm 3 \times 10^{-6}$
MX42	4689.28	Rd2	−8.18	4.05	$0.70821 \pm 3 \times 10^{-6}$
MX42	4671.20	Rd2	−8.36	4.80	$0.70790 \pm 9 \times 10^{-6}$
MX42	4690.6	Rd2	−8.07	3.82	$0.70824 \pm 5 \times 10^{-6}$
MX42	4671.68	Rd2	−8.14	5.44	$0.70765 \pm 5 \times 10^{-6}$
MX108	4687.18	Rd2	−8.47	4.32	
MX108	4671.52	Rd2	−8.00	4.99	$0.70792 \pm 6 \times 10^{-6}$
MX108	4689.56	Rd2	−7.83	4.00	$0.70818 \pm 6 \times 10^{-6}$
MX108	4670.80	Rd2	−8.83	4.91	
MX108	4670.70	Rd2	−8.25	4.73	$0.70807 \pm 2 \times 10^{-6}$
MX108	4689.45	Rd2	−8.21	4.42	$0.70847 \pm 5 \times 10^{-6}$
MX150	4502.56	Rd3	−7.23	5.52	$0.70726 \pm 5 \times 10^{-6}$
MX150	4503.84	Rd3	−7.15	4.51	
MX150	4504.43	Rd3	−8.16	3.23	$0.70776 \pm 3 \times 10^{-6}$
MX150	4505.88	Rd3	−8.45	3.64	$0.70750 \pm 6 \times 10^{-6}$
MX117	4605.20	Rd3	−7.96	4.08	$0.70782 \pm 4 \times 10^{-6}$
MX117	4607.36	Rd3	−7.84	4.35	
MX117	4608.52	Rd3	−8.79	4.87	
MX117	4609.56	Rd3	−9.30	3.82	$0.70815 \pm 2 \times 10^{-6}$
MX117	4612.33	Rd3	−7.84	4.05	$0.70793 \pm 4 \times 10^{-6}$
MX117	4614.35	Rd3	−7.92	3.24	
MX117	4615.13	Rd3	−8.26	3.45	
MX42	4652.36	Rd3	−7.72	3.46	$0.70793 \pm 6 \times 10^{-6}$
MX42	4658.25	Rd3	−8.23	4.28	$0.70843 \pm 3 \times 10^{-6}$
MX42	4653.46	Rd3	−8.56	3.97	$0.70797 \pm 3 \times 10^{-6}$
MX42	4657.65	Rd3	−7.68	3.75	$0.70853 \pm 6 \times 10^{-6}$
MX42	4659.34	Rd3	−9.86	3.65	
MX42	4658.03	Sd	−8.61	4.00	$0.70856 \pm 5 \times 10^{-6}$
MX42	4658.49	Sd	−8.55	3.94	$0.70837 \pm 2 \times 10^{-5}$
MX42	4658.27	Sd	−8.19	4.56	$0.70853 \pm 6 \times 10^{-6}$
MX42	4658.43	Sd	−8.55	4.43	$0.70811 \pm 4 \times 10^{-6}$
MX42	4652.99	Sd	−8.47	3.67	$0.70813 \pm 4 \times 10^{-6}$

coupled plasma mass spectrometry (Q-ICP-MS) coupled with an ASI Resolution LR 193 nm ArF excimer laser ablation (LA) system at Micro-Origin and Spectrum Laboratory. The sample spots were set to 120 μm. The laser time for the experiment was set with 3s surface cleaning, 7 s washout, 15 s background, 18 s of ablation, and 5s washout at 15Hz repetition rate and with a fluence of 3 J/cm². The standard NIST 614 glass were used as the primary reference materials. NIST 614 glass measurement was inserted in each of the 5test sets to correct the $^{207}Pb/^{206}Pb$ ratios, instrument drift and partial bias in the $^{238}U/^{206}Pb$ ratio (Woodhead and Hergt, 2001), but not for down-hole fractionation. $^{238}U/^{206}Pb$ ratios of calcite samples were then further calibrated with in-house standards (AHX-1d, ID-MC-ICP-MS calibrated, 236.9 ± 1.7 Ma, unpublished data) and cross-checked with ID-MS calibrated calcite standard Duff Brown Tank (64.0 ± 0.7 Ma, Hill et al., 2016). Moreover, an in-house intensive LA calibrated standard (LD-5, 72.5 ± 1.0 Ma) for age

Table 2
Rare earth elements and yttrium (REEY) concentrations (in ppm) of micrite limestone, Rd2, Rd3 and Sd of the Qixia Formation and modern Bahama ooids.

Samples	PY1-1	PY1-2	PY1-3	MX42-1	MX42-2	MX42-3	MX42-4	MX42-5	MX42-6	MX42-7	MX42-8	MX117-1	MX117-	MX117-	MX117-	MX42-9	Modern Bahama ooids[a]
Depth, m	6000.00			4652.50	4652.50	4652.50	4650.97	4650.97	4650.97	4651.50	4651.50	4603.57	4603.57	4603.57	4603.57	4651.50	
Lithology	Limestone	Limestone	Limestone	Rd2	Rd2	Rd2	Rd2	Rd2	Rd2	Rd3	Rd3	Rd3	Rd3	Sd	Sd	Sd	
La	0.625	0.437	0.525	0.301	0.297	0.299	0.199	0.202	0.216	0.156	0.139	0.225	0.242	0.105	0.200	0.116	0.159
Ce	0.391	0.269	0.322	0.527	0.512	0.493	0.390	0.401	0.360	0.254	0.262	0.385	0.374	0.203	0.350	0.204	0.185
Pr	0.084	0.062	0.066	0.065	0.061	0.052	0.046	0.045	0.037	0.032	0.027	0.045	0.044	0.025	0.049	0.020	0.041
Nd	0.300	0.242	0.281	0.250	0.220	0.228	0.173	0.175	0.114	0.110	0.133	0.186	0.150	0.086	0.175	0.089	0.205
Sm	0.039	0.045	0.048	0.027	0.023	0.034	0.029	0.037	0.022	0.014	0.025	0.026	0.021	0.015	0.023	0.012	0.063
Eu	0.014	0.013	0.011	0.012	0.005	0.005	0.007	0.006	0.005	0.003	0.003	0.006	0.004	0.003	0.005	0.002	0.019
Gd	0.071	0.067	0.056	0.042	0.039	0.043	0.031	0.022	0.030	0.030	0.012	0.035	0.027	0.014	0.032	0.011	0.110
Tb	0.010	0.009	0.009	0.006	0.005	0.004	0.003	0.003	0.003	0.002	0.002	0.005	0.003	0.003	0.003	0.003	0.018
Dy	0.074	0.071	0.063	0.045	0.045	0.040	0.027	0.026	0.024	0.027	0.022	0.041	0.037	0.026	0.032	0.017	0.129
Y	1.307	1.298	1.165	0.679	0.654	0.615	0.403	0.394	0.414	0.373	0.290	0.698	0.577	0.383	0.466	0.259	1.607
Ho	0.018	0.016	0.015	0.011	0.010	0.009	0.006	0.007	0.006	0.007	0.005	0.011	0.008	0.007	0.007	0.004	0.033
Er	0.048	0.048	0.045	0.041	0.037	0.026	0.022	0.024	0.017	0.017	0.016	0.032	0.028	0.027	0.019	0.010	0.102
Tm	0.007	0.005	0.006	0.007	0.005	0.005	0.002	0.003	0.003	0.003	0.002	0.005	0.004	0.003	0.003	0.001	0.013
Yb	0.038	0.035	0.041	0.040	0.035	0.029	0.023	0.024	0.015	0.017	0.016	0.035	0.017	0.019	0.016	0.007	0.074
Lu	0.006	0.005	0.006	0.007	0.006	0.005	0.003	0.003	0.002	0.003	0.002	0.005	0.003	0.003	0.002	0.001	0.011
REE	1.723	1.325	1.493	1.381	1.300	1.271	0.962	0.979	0.854	0.675	0.663	1.042	0.963	0.539	0.916	0.495	1.162
BSI	0.935	1.106	0.925	0.711	0.750	0.928	0.959	0.844	1.000	0.960	0.911	0.796	0.881	0.715	1.050	1.024	1.174
(Eu/Eu*)$_{SN}$	1.308	1.220	1.065	1.753	0.845	0.591	1.145	0.865	0.928	0.712	0.615	0.951	0.813	1.079	0.904	0.760	1.143
(Ce/Ce*)$_{SN}$	0.380	0.367	0.381	0.770	0.782	0.803	0.836	0.861	0.816	0.736	0.870	0.782	0.740	0.820	0.729	0.865	0.529
(Pr/Yb*)$_{SN}$	0.713	0.572	0.516	0.524	0.556	0.577	0.633	0.602	0.780	0.586	0.558	0.406	0.804	0.415	0.961	0.932	0.177

[a] Reference REEY compositions of Modern Bahama ooids from Li et al. (2019).

reliability and accuracy was utilized.

4. Petrography

4.1. Lithofacies

The Qiaxia Formation is generally composed of dolostones, limestones and siliceous limestones. The carbonate rocks in the middle-lower part of the Qiaxia Formation were commonly with well-preserved sedimentary structures and characterized by dark grey mud-limestone and grain-limestone with chert nodule and/or bioclast (Fig. 3a and b). These bioclasts are generally deepwater biological assemblages, such as planktonic foraminifera and coccolith and calcium spheres (Fig. 3c−f). In contrast, the carbonate rocks of the Upper Qixia Formation were moderately to extensively dolomitized as the thin-layered in the Central Sichuan Basin based on our core and thin sections examination (Fig. 4). The single layer dolostones were generally 1−3 m thick, with the abundance increasing of dolomites upwards (Fig. 4). The content of dolomite is related to the lithology of precursor carbonate. Thin sections observation exhibits that carbonate rocks are commonly dolomitized in lime-grainstone and bioclastic lime-packstone, and partly dolomitized to dolomitic limestone or calcareous dolomite in bioclastic lime-mudstone.

4.2. Dolomite petrography

Based on the crystal size, growth features, boundary shapes (planar and non-planar) and colors under CL microscope, two types of dolomites including matrix dolomite (RD) and cement dolomite (SD) were recognized in the Qixia Formation.

4.2.1. Very finely to finely crystalline dolomite (Rd1)

Rd1 in the core is commonly dark grey with fabric-retentive. It is nonporous and composed of very finely to finely anhedral to subhedral crystals varying from 10 μm to 100 μm (Fig. 6a). Rd1 displays a nonplanar-a to planar-s texture (Fig. 6a). Rd1 is less than 1 % by abundance and crosscut by stylolites in some samples. Rd1 was not sampled for geochemical analysis because of its low abundance and small crystal size in the study.

4.2.2. Finely to medium crystalline dolomite (Rd2)

Rd2 in the core is generally light grey to grey and widely distributed in study area. It is relatively porous and has sugar-like structures (Fig. 5a and b). The lithologies of Rd2 are mostly bioclastic wackestones and packstones which were partially to completely dolomitized (Fig. 6b and c). Rd2 comprised of finely to medium anhedral to subhedral crystals with sizes of 100−250 μm. The crystal of Rd2 exhibits a nonplanar-a texture and shows undulating extinction under cross-polarized light (Fig. 6d and e). The precursor carbonate grains, including chlorella and crinoids are well-preserved (Fig. 6b). In the locally silicified, Rd2 crystals are still enhedral when surrounded by the microstalline quartz. Under CL, Rd2 crystals are moderately bright red and bright red when they are near the pores (Fig. 6f).

4.2.3. Coarsely crystalline dolomite (Rd3)

Rd3 is commonly light grey in hand specimens (Fig. 5c and d) accounting for the highest proportion of total micrite dolomites. Generally, Rd3 is breccia-like due to a large number of needle-like pores or vugs up to several centimetres in diameter (Fig. 5e−h). Like Rd1 and Rd2, Rd3 is still fabric-retentive with preservation of the precursor grain fabric and textures. Rd3 crystals are mainly composed of medium to coarse crystalline, subhedral to euhedral crystals with sizes of 250−500 μm. It is usually transitional contact

Table 3
Inclusion data of Qixia Formation dolomites in central Sichuan Basin.

Type of dolomite	Number of samples	Homogenization temperature, °C		Number of samples	Salinity, w.t.% NaCl	
		Range	Avg.		Range	Avg.
Rd2	57	87.4—126.7	109.6	10	6.9—10.8	9.8
Rd3	18	110.0—146.0	121.5	14	7.8—11.4	9.7
Sd	12	128.7—152.9	136.7	7	8.4—11.5	10.2
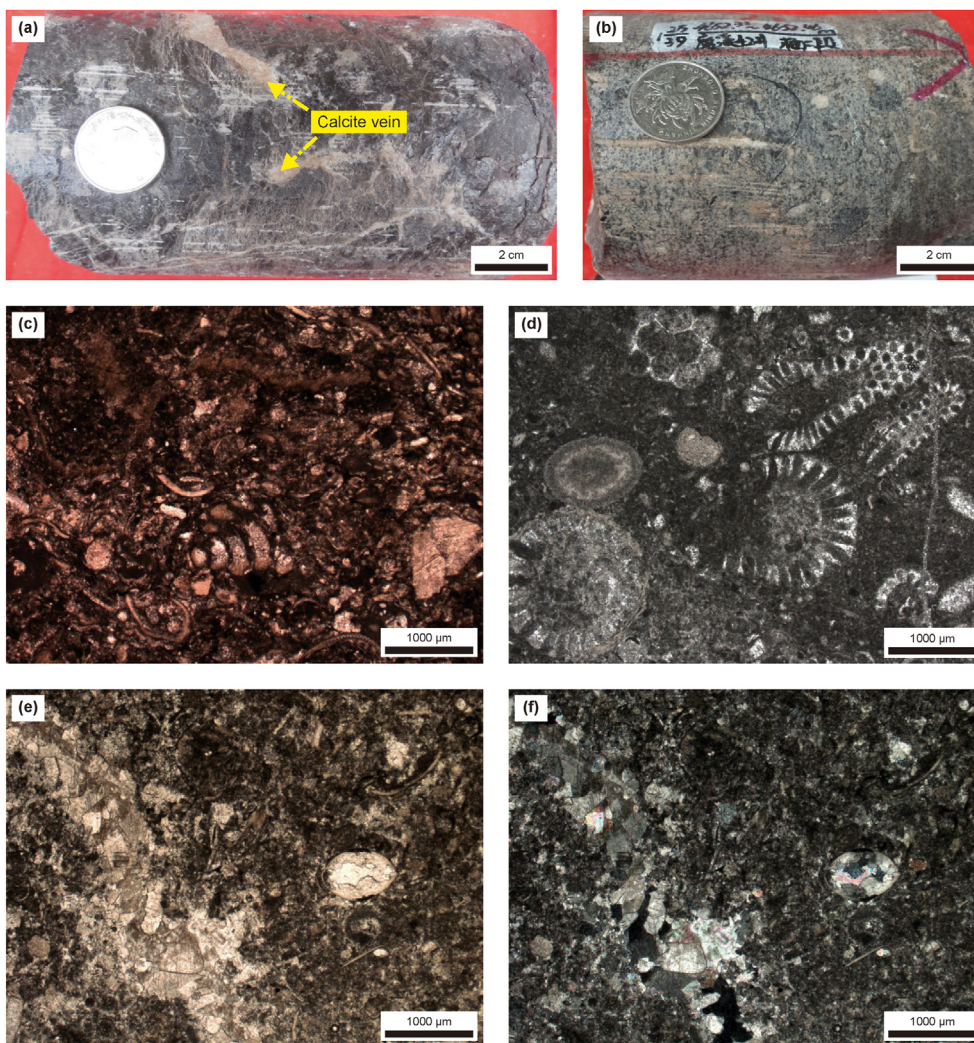
Fig. 3. Characteristics of limestone in Qixia Formation in central Sichuan Basin. **(a)** Grey to black lime-grainstone with abandant bioclastics, Well MX108, 4680.17—4680.33 m; **(b)** Dark grey bioclastic limestone, Well MX42, 4652.30—4652.39 m; **(c)** Abundant bioclastics were observed in lime-packstone, Well MX108, 4689.27 m; **(d)** Planktonic foraminifera and coccolith and calcium spheres were well preserved, Well MX42, 4652.30 m (+); **(e, f)** Saddle dolomite cement with wavy extinction filled the fracture in the bioclastic lime-packstone, Well MX108, 4679.65 m.

with Rd2, and exhibits a nonplanar-a texture with obvious undulating extinction (Fig. 6g—j). The crystals commonly have a hazy rhombic center surrounded by a clean rim (Fig. 6h and i). Locally, it can be observed that the crystals are surrounded by bitumen filled in the intercrystalline pores and solution pores (Fig. 6h and i). Under CL, Rd3 crystal shows moderately bright red color (Fig. 6l).

4.2.4. Saddle dolomites cement (Sd)

Sd filled the fractures or vugs in matrix dolomites as a milky white appearance in hand specimens (Fig. 5e—h). As the most cement by abundance, Sd exhibits coarse crystalline with crystal sizes greater than 500 μm. They are mainly observed as a nonplanar-a texture and show obvious undulating extinction under cross-polarized light (Fig. 6i). Sd crystals generally grew along the Rd2 and Rd3 (Fig. 6j—l) and display moderately bright red in the core area with dull red bands along the rim area under CL (Fig. 6l).

4.3. Hydrothermal minerals

Hydrothermal mineral assemblages such as quartz, fluorite and pyrite cements were observed in crystalline pores, vugs and fractures (Fig. 7). Nonetheless, they have relatively low abundance
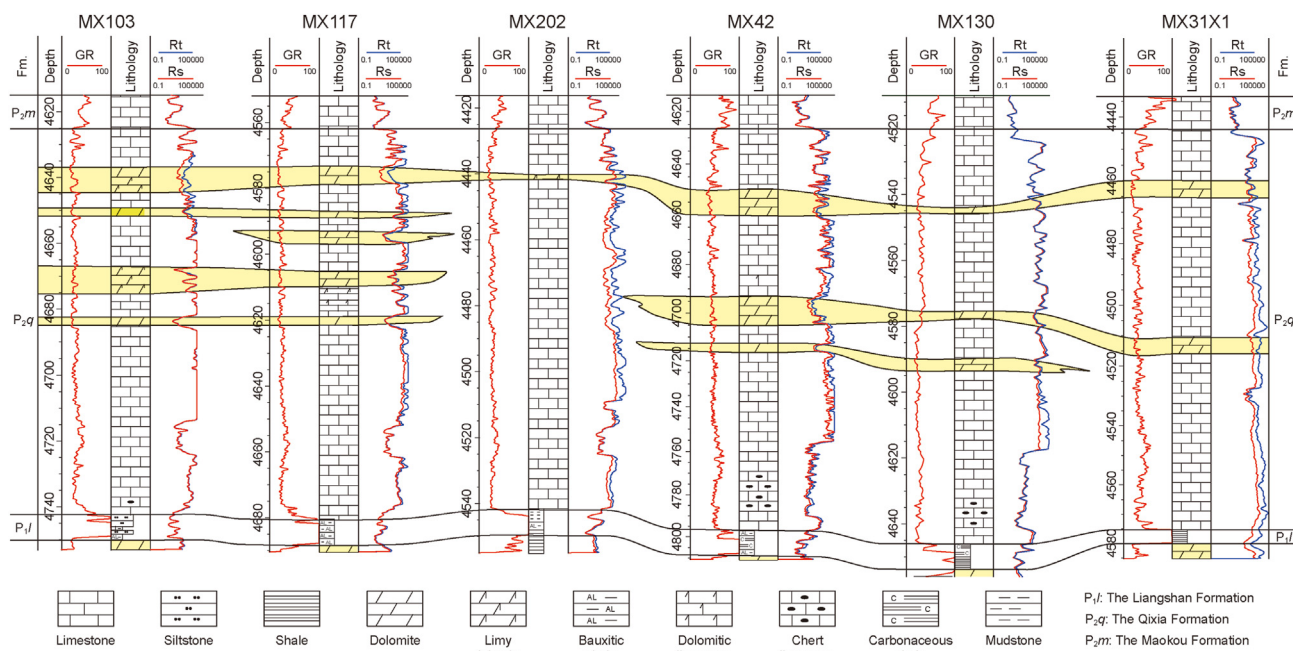
Fig. 4. Stratigraphic correlation of the Qixia Formation dolomites in the central Sichuan Basin.
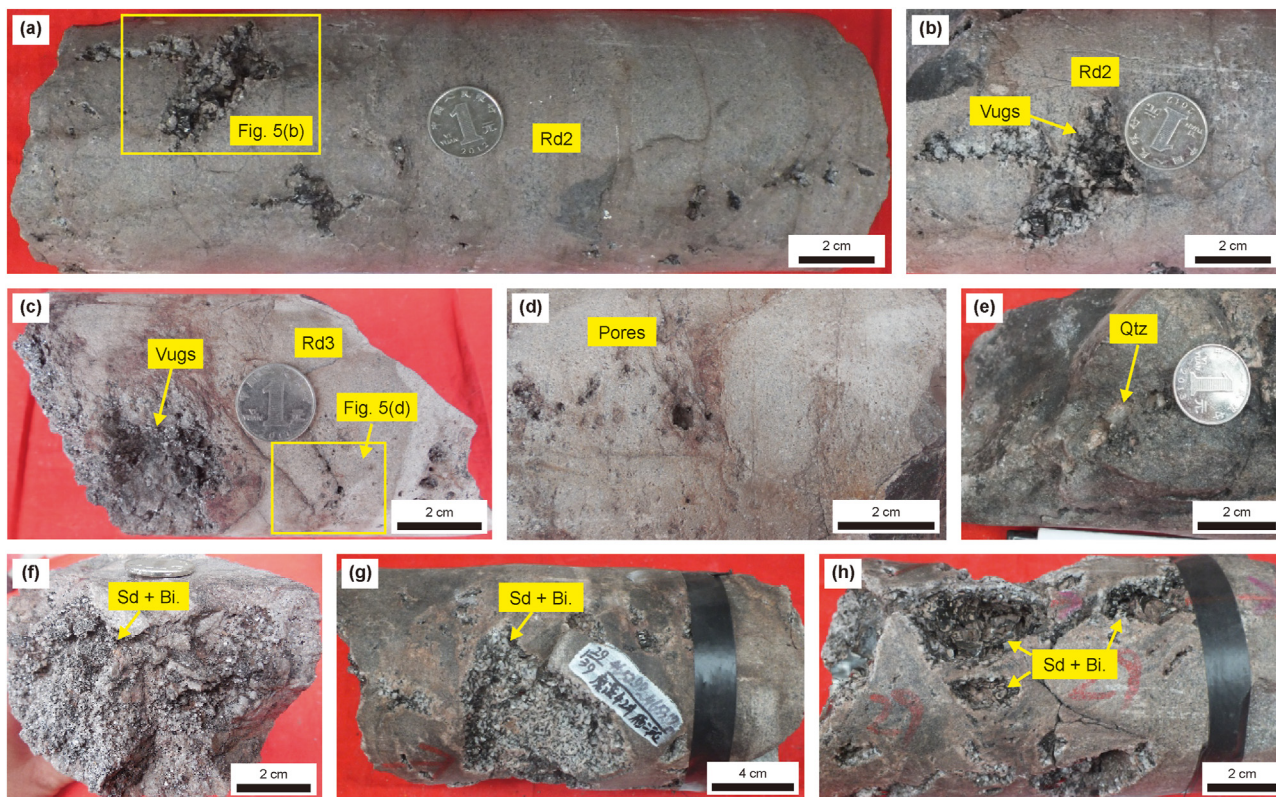

Fig. 5. Representative core photographs showing Rd2, Rd3 and Sd in the vugs of the Qiaxia Formation. in the Central Sichuan Basin. (**a, b**) Core photographs of Rd2 with a few vugs, Well MX108, 4651.75—4652.04 m; (**c, d**) Vugs and pinhole-like pores in Rd3, saddle dolomite cemnets grow along with Rd3, Well MX108, 4689.55— 4689.74 m; (**e**) Core photograph showing the paragenetic sequence from Rd3 dolomite, to Sd, bitumen and later quartz (Qtz), Well MX42, 4653.32—4653.46 m; (**f**) Saddle dolomites (Sd) in Rd3 vugs, with no sharp contacts, Well MX108, 4689.58 m; (**g**) Saddle dolomites covered with black bitumen (Bi.), Well MX42, 4652.99—4653.19 m; (**h**) Saddle dolomite veins with breccia-like texture of matrix dolomite, Well MX42, 4653.19—4653.32 m.

overall. They are found occasionally to coexist, and are often accompanied with Rd2, Rd3 and Sd (Fig. 7). Under CL illumination, the quartz crystals are generally non-luminescent (Fig. 7a—c). The chemical element compositions of fluorite and pyrite minerals have
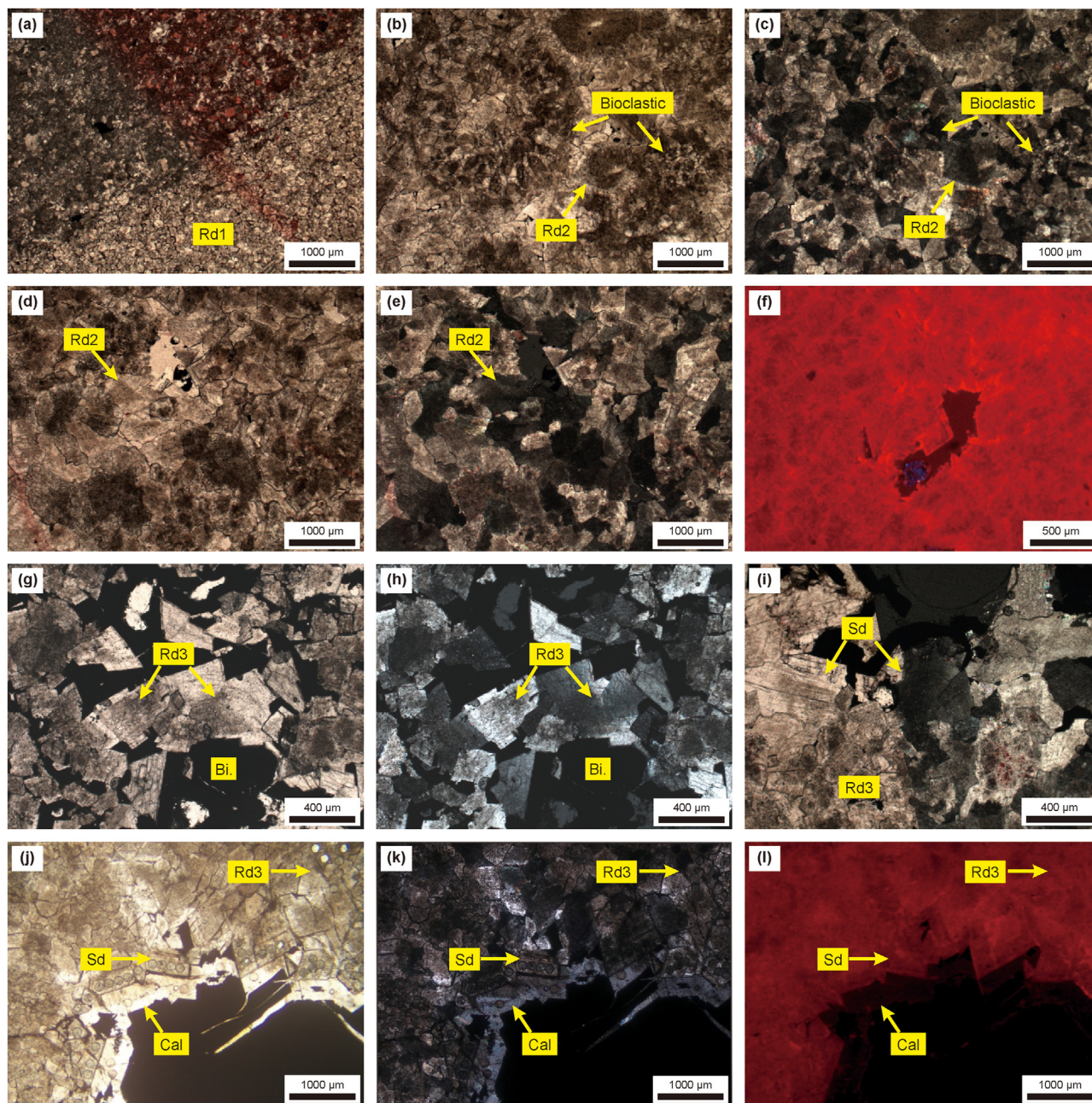
Fig. 6. Petrologic characteristics of dolomites and Sd. **(a)** Photomicrography of Rd1, micrite limestone partially to completely replaced by Rd1 along the stylolites, Well MX108, 4661.77 m; **(b, c)** Rd2 with bioclastic residues such as chlorella and crinoids showing wavy extinction, Well MX108, 4670.70 m; **(d, e)** Rd2 with bioclastic residues of chlorella with evident wavy extinction (red circle), Well MX108, 4671.20 m; **(f)** Rd2 crystals show moderately bright red color and bright red along pores under CL, Well MX42, 4652.01 m; **(g, h)** The crystals of Rd3 are dirty with a wavy extinction, and the pores are filled with bitumen, Well MX108, 4689.28 m; **(i)** Sd cement grows along Rd3, characterized by dirty crystal surface and wavy extinction, Well MX108, 4687.18 m; **(j, k)** Vugs filled by Sd, Cal (Calcite) cements and Bi. (Bitumen), Well MX42, 4651.5 m; **(l)** CL photomicrograph for (j and k) Rd3 and Sd, Rd3 dolomite shows moderately bright red luminescence and Sd has moderately bright red in the core area with dull red bands along the rim area, Well MX42, 4651.5 m.

been confirmed using SEM, surface scanning and EDX analysis (Fig. 7d–h).

5. Geochemistry

5.1. Isotope geochemistry

Measured C, O, and Sr isotopes from micrite limestone, Rd2, Rd3 and saddle dolomite cement are listed in Table 1 and illustrated in Figs. 7 and 8. The isotopes of Rd1 were not measured due to its low abundance. The micrite limestone has $\delta^{13}C$ (VPDB) of 2.42 ‰–5.02

‰ (mean values of 3.85 ‰, $n = 26$) and $\delta^{18}O$ (VPDB) values of −7.48 ‰ to −4.67 ‰ (mean values of −6.48 ‰, $n = 26$). The $^{87}Sr/^{86}Sr$ ratios of micrite limestones range from 0.70729 to 0.70822 (mean values of 0.70780, $n = 8$). The $\delta^{13}C$ (VPDB), $\delta^{18}O$ (VPDB) and $^{87}Sr/^{86}Sr$ ratios of micrite limestones are similar with those of the Permian marine calcite ($\delta^{13}C$ values of 0.0 to +6.0 ‰, $\delta^{18}O$ values of −7.5 ‰ to −1.5 ‰, and $^{87}Sr/^{86}Sr$ ratios of 0.70700−0.70850, Major et al., 1992; Veizer et al., 1999).

Rd2 show the $\delta^{13}C$ values ranging from 3.70 ‰ to 5.44 ‰, with an average of 4.50 ‰ ($n = 14$), which are similar with those of the micrite limestones. It shows $\delta^{18}O$ values ranging from −8.83 ‰
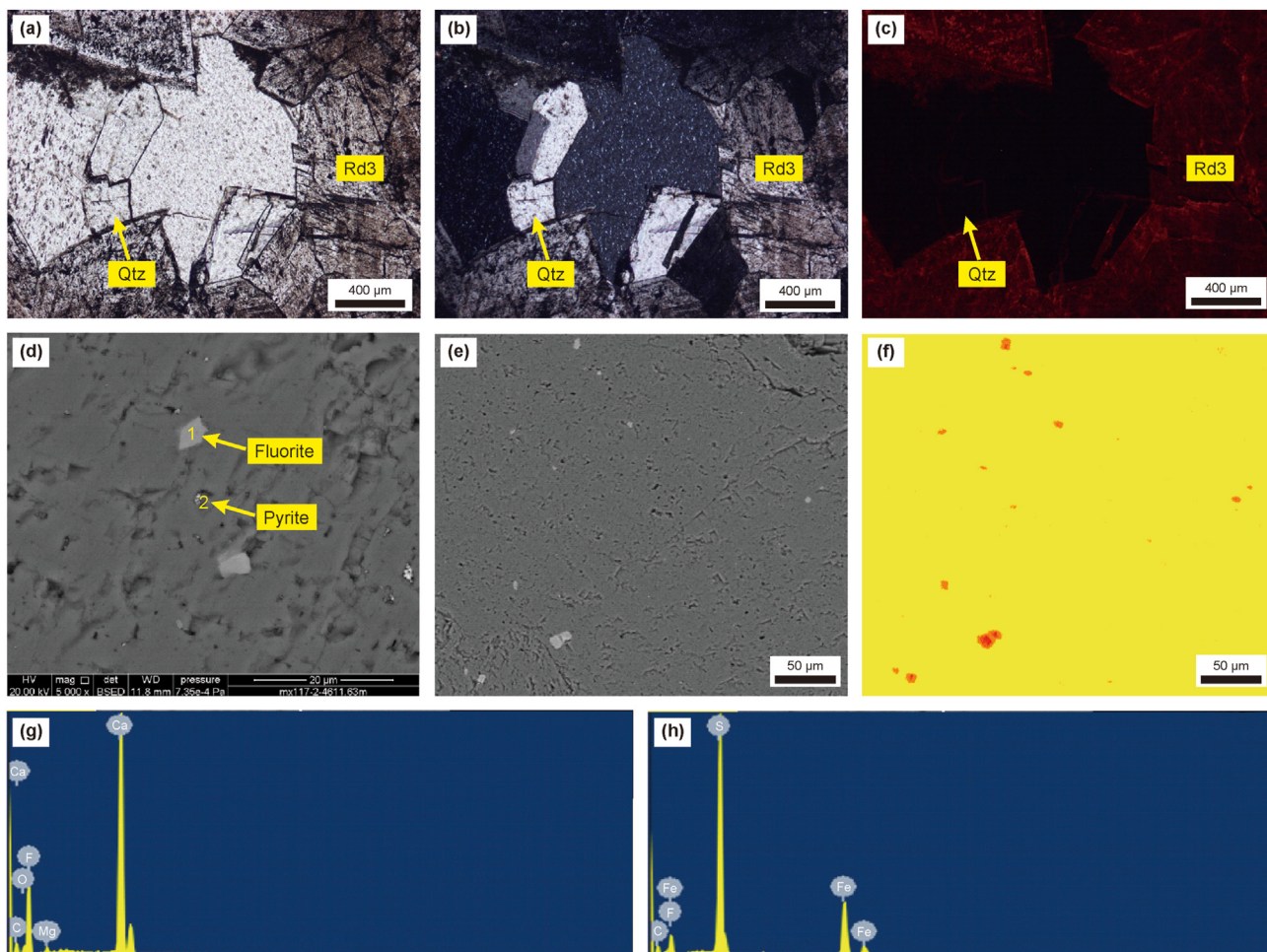
Fig. 7. Hydrothermal mineral assemblages of the Qixia Formation drilling cores. **(a, b)** Photomicrograph of quartz filling the intercrystalline pores of Rd3, Well MX42, 4651.5 m; **(c)** The quartz crystals is non-luminescent under CL, Well MX42, 4651.5 m; **(d)** Fluorite and pyrite under SEM, Well MX117, 4611.63m; **(e)** Fluorites widely scattered among the dolomite crystals, SEM, Well MX117, 4611.63 m; **(f)** Surface scaning of (e), the red color indicates the enrichments of F^-; **(g)** EDX analysis of the fluorite in (d); **(h)** The EDX analysis of the pyrite in (d).

to -7.83 ‰ (mean -8.25 ‰, $n = 14$), which are lower than those of the micrite limestones (Fig. 8). The $^{87}Sr/^{86}Sr$ ratios of Rd2 range from 0.70726 to 0.70853, with an average of 0.70811 ($n = 11$), which are slightly higher than those of the micrite limestones (Fig. 9).

The $\delta^{13}C$ values of Rd3 range from 3.23 ‰ to 5.52 ‰ (mean values of 3.99 ‰), similar to those of the micrite limestones, and the
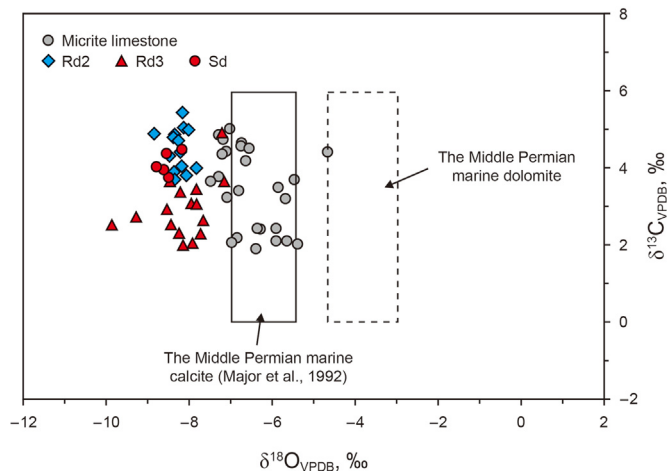
Fig. 8. A scatter diagram of $\delta^{18}O$ and $\delta^{13}C$ of the Qixia Formation carbonate rocks in the central Sichuan Basin.
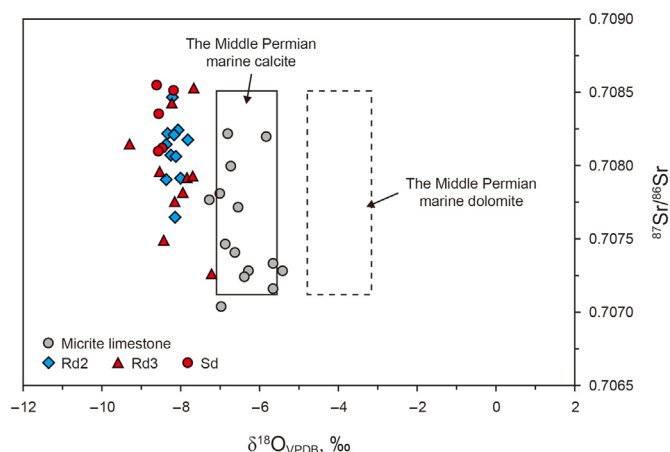
Fig. 9. A scatter diagram of $\delta^{18}O$ and $^{87}Sr/^{86}Sr$ ratios of the Qixia Formation carbonate rocks in the central Sichuan Basin.

$\delta^{18}O$ values of Rd3 range from -9.86 ‰ to -7.15 ‰ (mean values of -8.18 ‰, $n = 16$), which are lower than those of the micrite limestones (Fig. 8). The $^{87}Sr/^{86}Sr$ ratios of Rd3 show a wide range of $0.70726-0.70853$ (mean values of 0.70793, $n = 10$), showing slightly more radiogenic $^{87}Sr/^{86}Sr$ ratios than the micrite limestones (Fig. 9).

For saddle dolomite cements, the $\delta^{13}C$ values range from 3.67 ‰ to 4.56 ‰ (mean values of 4.12 ‰, $n = 5$), similar to those of micrite limestones. Sd show negative $\delta^{18}O$ values, ranging from -8.61 ‰ to -8.19 ‰ (mean -8.47 ‰, $n = 5$) (Fig. 8). The $^{87}Sr/^{86}Sr$ ratios of Sd show a narrow range varying from 0.70811 to 0.70856 (mean 0.70834, $n = 5$) (Fig. 9).

5.2. Trace elements

The trace element values of micrite limestone ($n = 4$), Rd2, Rd3 and Sd dolomites in the Qiaxia Formation are summarized in Table 2, and their REEY patterns are illustrated in Fig. 10. The total rare earth element concentration (ΣREE) of the micrite limestone samples range from 1.33 ppm to 2.90 ppm (mean values of 1.86 ± 0.61 ppm). The REEY patterns are characterized by (1) negative Ce ($0.37-0.38$, 0.37 ± 0.006), (2) superchondritic Y/Ho ratios ($65.08-80.21$, 73.99 ± 5.79), and (3) LREE depletion relative to HREE (($Pr/Yb)_{SN} = 0.52-0.71$, 0.60 ± 0.07) (Fig. 10a).

All the Rd2, Rd3 and Sd samples show relatively low ΣREE, of 0.85 ppm-1.38 ppm (mean values of 1.12 ppm, $n = 6$), 0.66 ppm-1.04 ppm (mean values of 0.84 ppm, $n = 4$), and 0.50 ppm-0.92 ppm (mean 0.65 ppm, $n = 3$), respectively. They are characterized by LREE depletion relative to HREE (($Pr/Yb)_{SN}$ of $0.41-0.96$, 0.64 ± 0.61), negative Ce anomaly, positive Y anomalies ($2.11- 2.73$, 2.45 ± 0.67), high Y/Ho ratios ($51.34-71.55$, 63.02 ± 23.76) (Fig. 10b$-d$). The Ce/Ce* ratios of all the dolomite samples range from 0.73 to 0.87 (0.80 ± 0.17) and most of the Pr/Pr* ratios are >1, indicating a true negative Ce anomaly (Bau and Dulski, 1996) (Fig. 11a). The high Y/Ho ratios of dolomite samples and Sd are within the values of seawater (Bau and Dulski, 1996)

(Fig. 11b). Additionally, all the dolomite samples have slightly negative Eu anomalies ($0.59-1.75$, 0.92 ± 1.03) (Table 2). The negligible correlation between Ce/Ce*, BSI and REE suggests that the REE of the carbonate samples is convinced and not modified by recrystallization (Fig. 11c and d).

In summary, the overall REEY patterns of Rd2, Rd3 and Sd are similar to the seawater-like proxies, except slightly lower HREE than what is in micrite limestones (Fig. 10). The seawater-like REEY signatures may be inherited from seawater, formation water originated from seawater or meteoric water dissolved host carbonate (Bau et al., 2003).

5.3. Fluid inclusions

Liquid-dominated biphase aqueous inclusions (with vapor percentage <50%) distributed in the growth zone were measured in Rd2 (Fig. 12a), Rd3 (Fig. 12b and c) and Sd (Fig. 12d$-f$). The T_h values of the Rd2 inclusions ranged from 87.4 °C to 126.7 °C ($n = 57$), and relatively low salinities with a range of 6.9-10.8 w.t.% NaCl equivalent (mean 9.8 w.t.% NaCl equivalent). The Rd3 and Sd inclusions had higher T_h values varying from 110.0 °C to 146.0 °C ($n = 18$) and 128.7 °C-152.9 °C, respectively. However, the salinities of Rd3 and Sd were close to those of Rd2 (Rd3: 7.8-11.4 w.t.% NaCl equivalent; Sd: 8.4-11.5 w.t.% NaCl equivalent) (Table 3 and Fig. 13).

5.4. Dolomite in situ U-Pb dating

The LA-ICP-MS U-Pb ages were successfully obtained from Rd3 and Sd (Fig. 14a and b) and the results are presented in Fig. 6j, k and l. The Rd3 sample generated a U-Pb age of 276.0 ± 5.4 Ma (Fig. 14a), which is basically consistent with the age (274.5 ± 9.9 Ma) tested by the other scholar (Duan et al., 2021). In addition, He et al. (2022) tested the matrix dolomites and reported the U-Pb ages 286 ± 10 Ma and 256 ± 12 Ma. Therefore, the U-Pb age is convinced and represents the forming time of Rd3. The Sd sample yielded a U-Pb age of 271.0 ± 5.6 Ma (Fig. 14b). Duan et al. (2021) measured the
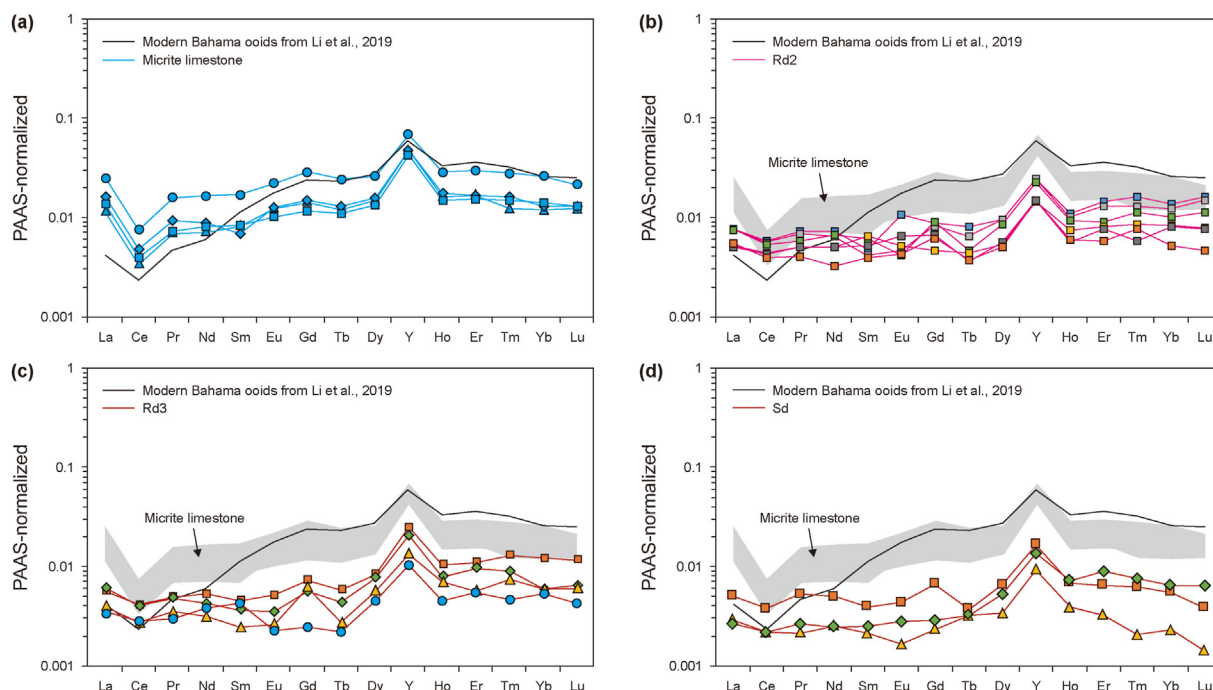

Fig. 10. PAAS-normalized REEY patterns of micrite limestone, Rd2, Rd3, and Sd in the Qiaxia Formation; The REEY data of modern Bahama ooids are from Li et al. (2019).
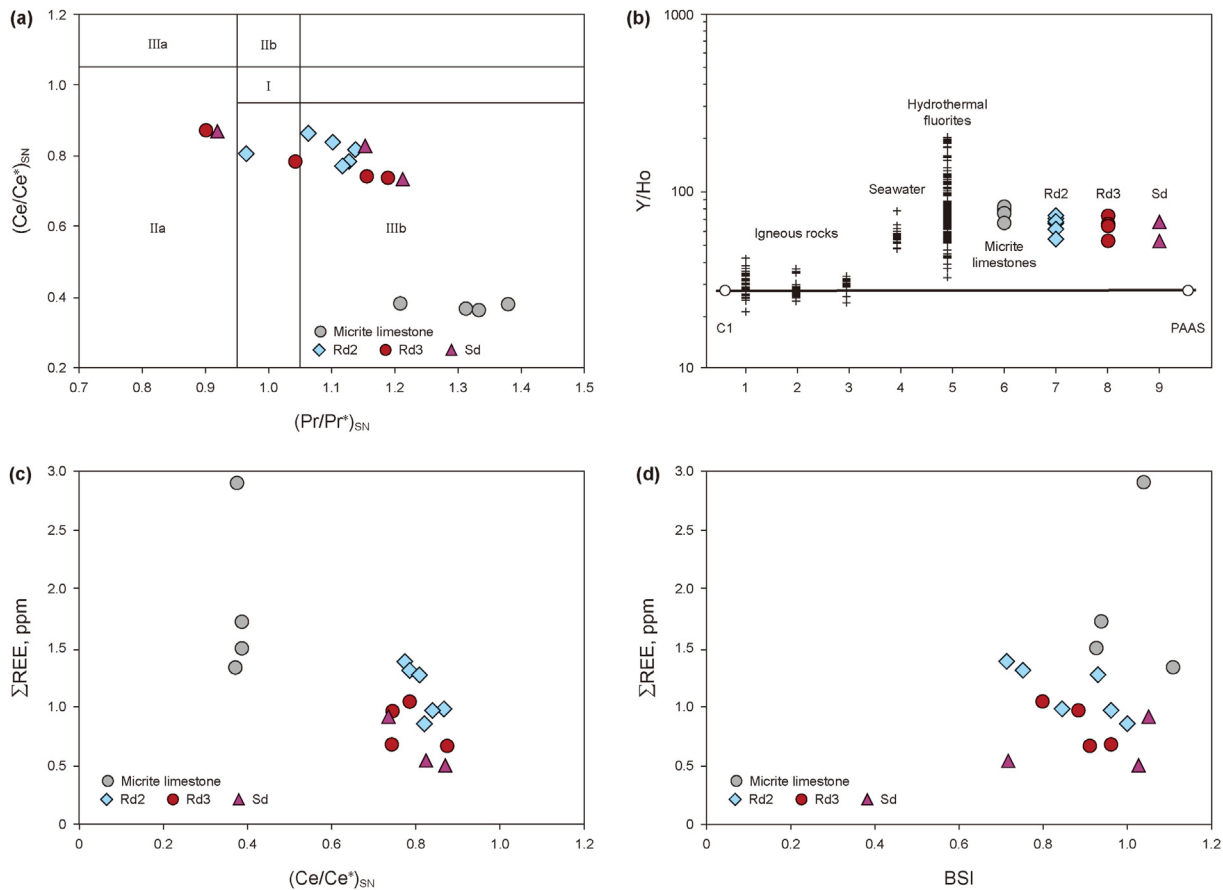
Fig. 11. (a) Diagram discriminating between La and Ce anomalies (after Bau and Alexander, 2009); (b) Y/Ho ratios of igneous rocks (l, 2, 3), South Pacific seawater (4), hydrothermal vein fluorites (5) and carbonate in this study (6–9) (after Bau and Dulski, 1995); (c) Cross plot between Ce anomaly and ΣREE, showing a negligible correlation; (d) Cross plot between BSI and ΣREE, showing a negligible correlation.
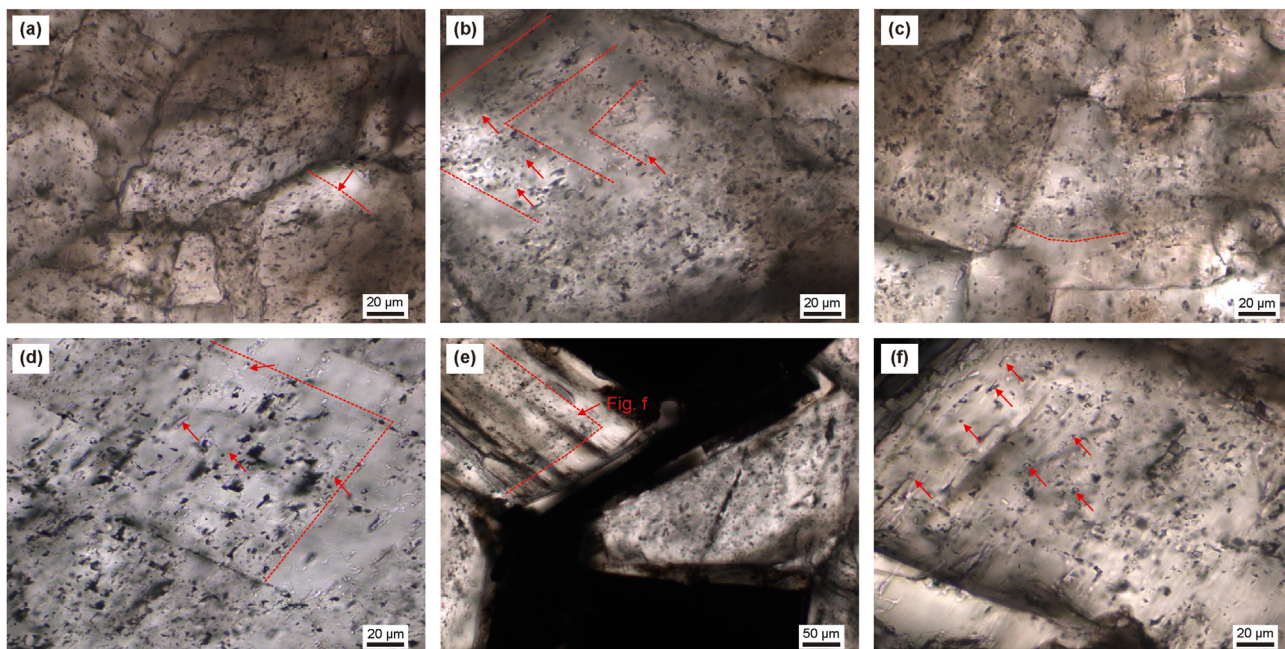

Fig. 12. Photomicrographs showing fluid inclusion petrography. (a) Fluid inclusions outlined the growth zone in the core of Rd2, MX42, 4690.60 m; (b, c) Liquid-dominated fluid inclusions coexist in growth zone, Rd3, MX108, 4671.20 m; (d) Photomicrograph showing two-phase primary aqueous in Sd, MX108, 4687.18 m; (e, f) Liquid-dominated fluid inclusions detected in the Sd of the dissolved pores, Well MX42, 4671.20 m.
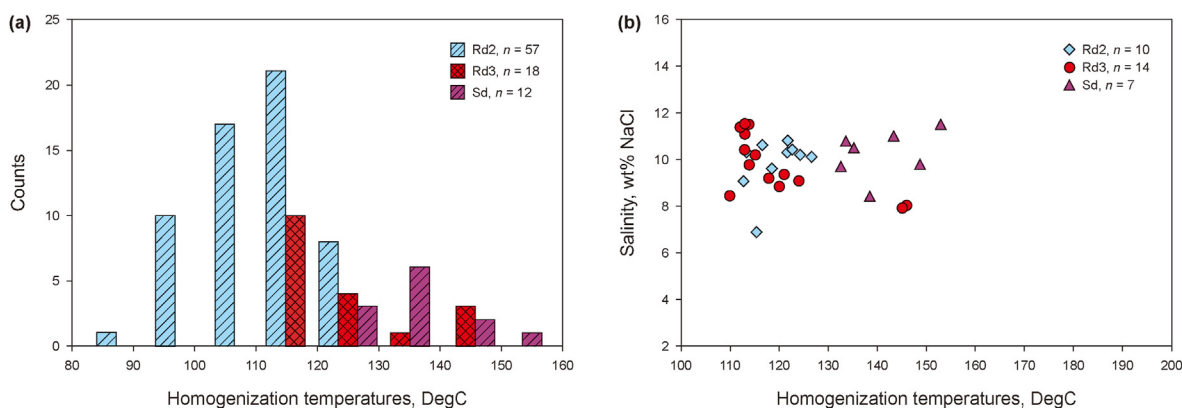
Fig. 13. **(a)** Histogram of homogenization temperature of Rd2, Rd3 and Sd in the Qixia Formation; **(b)** Cross-plot of salinity versus homogenization temperatures (T_h) from fluid inclusions of Rd2, Rd3 and Sd.
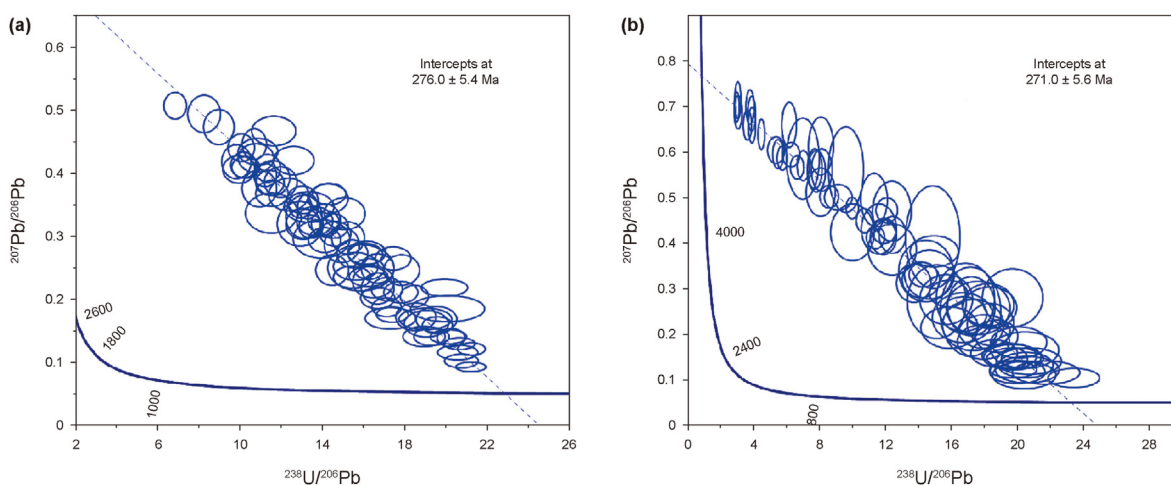

Fig. 14. Tera-Wasserburg Concordia diagrams showing $^{238}U/^{206}Pb$ versus $^{207}Pb/^{206}Pb$ of Rd3 (a) and Sd (b).

Sd sample of Well MX108 and obtained a U-Pb age of 262.7 ± 7.5 Ma.

6. Discussion

6.1. Dolomite forming environment

In the study area, dolomites generally occur in bioclastic limestone in the Qiaxia Formation. The multilayered cyclic distribution of dolomites in the vertical sedimentary sequence indicates that dolomitization is closely related to the grain-rich lithofacies deposited in moderate to high water energy of transgressive portions. We proposed, that Rd2 and Rd3 mainly replaced the lime-packstones and grainstones in a high temperature environment during the shallow buried stage. Lines of evidences are as follow.

Firstly, Rd2 and Rd3 partly preserve the precursor fabrics (Fig. 6b and c), including original characteristic and precursor carbonate grain structures (chlorella, crinoids stems and other bioclasts are observed) according to the microscopic observation. In addition, the edge-bright grains around the pores are bright red under CL (Fig. 6f), suggesting that the dolomite may have been formed in early stage that rich in Mn and poor in Fe. The Rd3 may develop slightly later than Rd2 because the Rd3 crystal often had a blurred boundary with the Rd2. These pieces of evidence indicate that Rd2 and Rd3 were probably formed in the early diagenesis. Rd2 and Rd3

crystals have curved crystal plane textures, dirty crystal surfaces and wavy extinction, indicating that they grew rapidly at a high temperature environment.

Sd crystals grow along the edges of fractures and vugs (Fig. 5f–h) and generally have blurred boundaries with Rd2 and Rd3 (Fig. 6i and j), indicating that they are interrelated during dolomitization. The breccia-like dolomites were generally developed along tensional faults or strike slip faults associated with the Emeishan large igneous province (ELIP). Moreover, faults as the conduit considerably channeled deep hydrothermal fluids, and the hydrothermal activity may be related to ELIP. Therefore, it further suggests that the formation of Sd was associated with high temperature fluid of the ELIP associated fluids.

6.2. Relation between strike-slip/extensional faults and dolomite distribution

During the Middle-Late Permian, many high-angle strike-slip and extensional faults began to develop due to the intense tectonic activities in the western-central Sichuan Basin (Yin et al., 2013). Based on drillings, seismic interpretation, and previous reported research results (Chen et al., 2012), it appears that two groups of strike-slip or extensional faults (SE-NE and NE-SW) developed during the Late stage of the Middle Permian. The high-angle extensional faults have evident throws.

As the products of the hydrothermal activity, silica, Mg-rich hydrothermal minerals (e.g. steatite) and limy mudstone horizontally distributed in the biological strata have been widely observed in the Mao 2 Member (Wang et al., 2014; Huang et al., 2014; Song et al., 2022). As lithology localized onto the faults, massive dolostone developed widely along strike-slip and extensional fault planes. Likewise, hydrothermal minerals (such as fluorite, pyrite, and sphalerite) scattered in dolomite crystals were observed (Fig. 7). When the strata were away from the fault planes, dolomites were characterized by thin-bedded with their precursor lime-packstone (Fig. 4). Consequently, the closer the strata to the fault, the thicker the dolomite was. Comprehensively, the strike-slip and extensional faults might have provided the pathways for hydrothermal fluids in forming the shoal-facies dolomites of the Qixia Formation.

6.3. The nature of dolomitization fluid and the dolomitization mechanism

6.3.1. Formation of Rd2

Rd2 is interpreted to have formed at high temperature shallow burial conditions by replacing residual calcite or by recrystallization of Rd1. Primary aqueous inclusions within the Rd2 reveal Th values that range from 87.4 °C to 126.7 °C (Fig. 13a). As described above, the Rd2 has been replaced by Rd3 and thus pre-dates them (276.0 ± 5.4 Ma). The age of Rd2 together with the burial history curve suggest that it has been formed at the shallow burial stage, and the burial temperature may be lower than 40 °C (Fig. 15). The dolomitization fluids forming Rd2 were significantly hotter than the formation temperature, indicating a hydrothermal origin. According to fluid-inclusion Th and $\delta^{18}O$ of the Rd2, the calculated $\delta^{18}O$ (SMOW) compositions of the parent fluids range from 0.2 ‰ to 5.8 ‰, with a positive shift relative to the Middle Permian seawater (Fig. 16). The $\delta^{18}O$ enrichment is likely due to either modified seawaters having experienced high temperature during the burial diagenesis or influx external $\delta^{18}O$-enriched hydrothermal fluids. Moreover, the $^{87}Sr/^{86}Sr$ ratios of Rd2 generally fall into the similar range recorded in the host rock (Fig. 9), indicating that the Rd2 likely resulted from marine-derived formation waters heated and/or mixed hydrothermal fluid to some extent.

During the process of fluid migration to mineral precipitation, the negative Ce anomaly, slight Eu negative anomaly and high Y/Ho ratios could be ascribed to two reasons: (1) the fluid itself has similar characteristics of rare earth elements; (2) Rare earth elements are fractionated during fluid migration (Bau et al., 2003). The homogenization temperature of fluid inclusion and slightly negative Eu anomaly indicate that Rd2 was formed in high temperature environment. Therefore, it was considered that dolomitization fluid had negative Ce anomaly and high Y/Ho ratios. A plausible explanation is a direct precipitation from slightly modified connate seawaters, as suggested by seawater-like REE patterns in fluid of the Rd2 relative to seawaters. The dolomitization fluids are more saline than normal seawaters (Fig. 13b), which can be interpreted as the result of the Middle Permian connate becoming saltier by interacting with ambient rock or mixing some deep hydrothermal.

Rd2 ages suggest that the dolomite distributed along the extensional and strike-slip faults associated with the ELIP. This correlates well with seismic interpretation, exploration and development results. The well-preserved original sedimentary structure and precursor carbonate grain indicate the dolomitization was controlled by sedimentary facies. Therefore, the dolomitization fluid of Rd2 might originate from the connate seawater mixed deep hydrothermal fluid communicated by faults to some extent. More specifically, during the early buried stage, the connate seawater in the porous strata heated and/or mixed with deep hydrothermal

fluid, occurred dolomitization and formed Rd2.

6.3.2. Formation of Rd3 and Sd

Rd3 and Sd are believed that have a similar fluid origin with Rd2 during different stage of the long-lasting hydrothermal event. This assumption originates from the following observations: (1) Rd3 might result from recrystallization of precursor Rd2, due to the crystal of Rd3 was generally in mixed development with Rd2 in the formation. Sd crystals generally have conformable contact with Rd2 and Rd3, showing they are formed in different stage. Rd3 and Sd crystals exhibit undulating extinction, indicating that Rd3 and Sd formed at high temperature burial conditions by modified seawater and/or deep hydrothermal fluid. (2) The carbon, oxygen and strontium isotopes of Rd3 and Sd are similar to those of Rd2 (Figs. 7 and 8). It is worth noting that the $\delta^{13}C$ and $^{87}Sr/^{86}Sr$ of Rd2, Rd3 and Sd are falling into the range of the micrite limestones. (3) All of the Rd2, Rd3 and Sd have the seawater-like REE patterns (Fig. 9). (4) According to the dolomite-water equation from Land. (1983), the $\delta^{18}O$ values of Rd3 and Sd dolomitizing fluids are 2.0−8.3 ‰ (VSMOW) and 5.2−7.9 ‰(VSMOW), respectively (Fig. 14). These petrological and geochemical evidences suggest Rd2, Rd3 and Sd may have the similar fluid origin.

Alternatively, the variation of geochemical characteristics indicates that dolomitization and Sd cement were formed in different stages. As revealed by petrological and U-Pb results, Rd3 (U-Pb age is 276.0 ± 5.4 Ma) and Rd3 (U-Pb age is 271.0 ± 5.6 Ma) are developed just slightly later than Rd2. This reflects that dolomitization and Sd cement might occur in the different stage of ELIP during the period from the Late Qixia Formation to the Early-Middle Maokou Formation. In the period, the upwelling of mantle plume caused the regional stretching, and a series of strike-slip faults began to develop. The hydrothermal fluids migrate upward along the faults and preferentially flow into lime-grainstone with high porosity and permeability. Therefore, the dolomitization and Sd cement developed as the connate seawater was heated and/or mixed deep hydrothermal fluid. Other Sd U-Pb ages such as 262.7 ± 7.5 Ma (Duan et al., 2021) and 252.9 ± 2.9 Ma (Lu et al., 2024) have been reported, indicating that saddle dolomite has undergone a long precipitation process.

Gradually increasing homogenization temperature from Rd2 (87.4−126.7 °C), Rd3 (110.0−146.0 °C) and Sd (128.7−152.9 °C) have been recorded, which all have similar medium salinity higher than seawater. The higher paleotemperatures of Rd3 and Sd imply deeper burial or heating effect of the hydrothermal event, in contrast to Rd2. However, the salinities exhibit no significant correlation to homogenization temperatures, indicating that the fluids of dolomitization and precipitating Sd were heated by hydrothermal activity of the ELIP rather than the burial depth. Based on the U-Pb ages and the burial history curve, the estimated burial depth was no more than 200 m apparently pointing to a hydrothermal origin (Fig. 15).

In addition, from the perspective of in-situ rare earth element characteristics, the ΣREE shows a gradually decreasing feature from Rd2 (0.85−1.38), Rd3 (0.66−1.04) to Sd (0.50−0.92) (Figs. 9 and 10). The decreasing REE content indicates that the rare earth in the fluids is gradually consumed and not supplemented during the formation of Rd2, Rd3 and Sd. Therefore, it was considered that hydrothermal activity led to elevated heat-flow conditions, thereby triggering the dolomitization and precipitation of dolomites. Rd2 and Rd3 were developed at different times during a hydrothermal event of ELIP. When the fracture-vuggy reservoir developed, the heated formation water began to crystallized and formed Sd.

6.3.3. Dolomitization mechanism

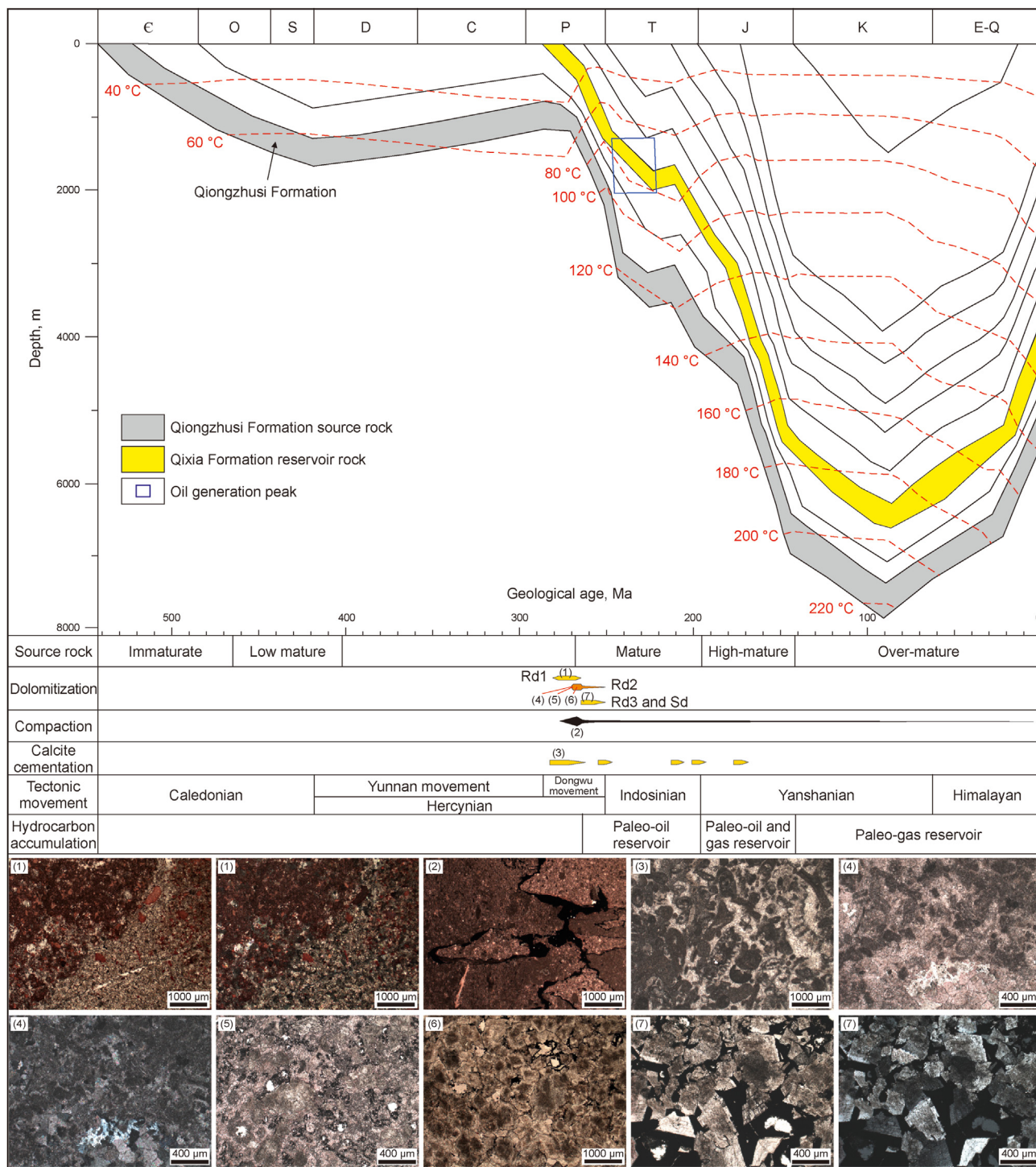According to the lithofacies and fluid origin analysis of different

Fig. 15. Burial history and diagenetic sequence of the Qixia Formation dolomites in the central Sichuan Basin. (1) Rd1 dolomitization front in limestone is constrained by a stylolite, Well MX108, 4661.77 m; (2) Stylolite is filled with bitumen, Well MX108, 4663.08 m; (3) The lime-grainstone was blocked by early calcite cement, Well MX42, 4659.01 m; (4) Hydrothermal siliceous mineral in the Rd2, Well MX42, 4650.1 m; (5) Dolomitization occurred along with early hydrocarbon charging, Well MX42, 4671.20 m; (6) The Rd2 is well-preserved the sedimentary structures and precursor carbonate bioclastic structures, Well MX42, 4658.43 m; (7) Bitumen formed after Rd3 and Sd, Well MX42, 4689.28 m.

dolomites and saddle dolomite cement, the dolomitization model was proposed in the Qixia Formation. Firstly, the lithology of the Qixia Formation with grey sparite bioclastic limestone (such as chlorella, echinoderms and coral debris) indicates a fluctuating open platform sedimentary environment with moderate water energy under a transgressive setting (Fig. 2), rather than pene-contemporaneous dolomitization of restricted environment (Li

et al., 2020; Lu et al., 2020). Secondly, all major dolomites retained original structure and mainly replaced the grainstones and/or packstones developed in bioclastic shoals. This differs from the dolomitization process associated with stylolites of compaction in buried environments (Jiang et al., 2009), except for the Rd1 dolomites that constitutes a relatively small volume. Additionally, the presence of hydrothermal dolomites confirms that the origin of the
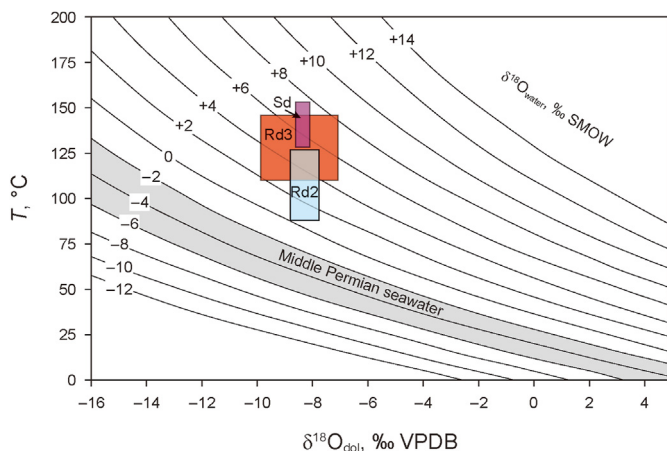
Fig. 16. Temperatures (*T*) versus δ^{18}O diagenetic fluid for δ^{18}O values of Sd using the dolomite-water equation $(10)^3$ lnαdolomite-water = 3.2×10^6 T^{-2}–3.3 (Land, 1983). The δ^{18}O of the Middle Permian seawater is the δ^{18}O of calcite from Veizer et al. (1999).

hydrothermal dolomites affected by the intensive volcanism related to the ELIP during the last Middle Permian. The southwest Sichuan basin is near the eruptive center of the ELIP. Hence, the zebra structure and saddle dolomite cement controlled by both faults and sedimentary facies are well developed in the southwest Sichuan Basin. The tectonic activity lasted until the Late Triassic in the edge of the Sichuan Basin (Huang et al., 2012, 2014; Li et al., 2016; Pan et al., 2021), resulting the time differences of hydrothermal dolomitization in the different areas.

The Rd3 and Rd2 crystals often had blurred boundaries and were interrelated and interdependent and distributed together (Fig. 6c–e), and retained original structure with wavy extinction apparently (Fig. 6d–h). The Sd filled in the pores, vugs and fractures generally adjoined the Rd2 or Rd3 crystals (Fig. 5f–h). The centers of pores and vugs were filled with bitumen, which suggested that the formation of palaeo-oil reservoir was later than that of the saddle dolomite (Fig. 5f–h and Fig. 6g–j). It is believed that the oil and gas in the Qixia Formation were generated mainly from the underlying Qiongzhusi Formation source rock (Wen et al., 2021). The burial and thermal history shows that the Qiongzhusi Formation source rocks began to generate oil in the Late Permian (Fig. 15), reached the peak of oil generation in the Early Triassic, and began to generate gas in the Middle-Late Jurassic (Wen et al., 2021). Furthermore, the U-Pb dating test have defined the time of dolomitization and Sd cement which might mainly developed before 271 ± 5.6Ma. In other words, the hydrothermal event occurred mainly from the Late Qixia Formation to the Early-Middle Maokou Formation. During this period, the burial temperature was lower than 40 °C (Fig. 15). Therefore, the high inclusion homogenization temperatures of Rd2, Rd3 and Sd indicate that dolomitization and Sd cement were ascribed to the elevated heat-flow triggered by hydrothermal event during the ELIP.

After determining the U-Pb ages, lithological characteristic and fluid sources of Rd2, Rd3 and Sd, as well as the dolomitization model controlled by both of faults and sedimentary facies was established. At rift initiation of ELIP, multiple strike-slip and extensional faults began to develop, and the fluid flux might have been controlled largely by geothermal convection, resulting in fabric-retentive Rd2 in precursor lime-grainstone with a well seawater-like proxy geochemistry. At that time, the burial depth of might be not more than 100m (Fig. 15). At rift climax, intense

structure deformation might cause the hydrothermal temperature increased and faults breached surface. Under this condition, cool seawater was drawn into convection cells along fault plane, heated by elevated heat-flow or mixed with hot, rising deep hydrothermal and form massive dolostone along fault plane. After that, the mixing hydrothermal fluids and seawater convected into the porous lime-grainstone strata or Rd2, resulting in dolomitization.

The dolomites were most developed near the fractures or faults, because the magmatic hydrothermal might be directly involved in dolomitization. Under this condition, dolomites are usually brecciated, and hydrothermal minerals such as fluorite, pyrite and sphalerite widely scattered in dolomite crystal (Fig. 17). Away from the fractures or faults, the formation water driven by temperature and pressure of the lime-grainstone and lime-packstone triggered dolomitization and formed the thin-bedded facies-controlled dolomites. This phenomenon also explains the fluid nature and geochemical characteristics are significantly different as the distance increases between the dolomites and faults (Fig. 17). The massive eruption of magma caused a sudden rise of the formation fluid temperature and further broke the binding affect of magnesium ion hydrate (Davies and Smith, 2006). In addition, the rapid upwelling of hydrothermal fluid brought a large quantity of magnesium-rich fluid to induce dolomitization near the fault (Guo et al., 2016), and increased the formation pressure, which drove the formation water to flow in the grainstone, resulting in extensive hydrothermal dolomitization.

7. Conclusions

Intraplatform shoal dolomite of the Qixia Formation is universal in the central Sichuan Basin, with vertically thin single layer and multilayer superpositions in cyclical distribution. The dolomites are classified as Rd1, Rd2 and Rd3. Rd1 comprises less than 1 % of the dolomite rocks by volume and cannot be sampled for geochemical analysis due to its scarcity and small crystal size. Rd2 and Rd3 retained their original sedimentary texture and dolomite crystals with wavy extinction. The thickness change of the dolomite is closely related to the distribution of faults, and the distribution corresponds closely with the distribution of intraplatform shoal facies. Coarsely crystalline saddle dolomite (Sd) with distinct wavy extinction often has blurred boundaries with Rd3 or Rd2, and grew along the edges of fractures and vugs of the breccia-like dolomite.

U-Pb ages from Rd3 and Sd cement indicate that the hydrothermal event was associated with the ELIP. The lithological and geochemical characteristics indicated that the dolomitization fluids originated from connate seawater heated by elevated heat-flow or mixed hydrothermal to some extent. Multiple extensional and strike-slip faults triggered by ELIP caused formation pressure and temperature rise which drove the connate seawater to flow into the lime-grainstone with great physical properties. These connate seawater with high temperature and pressure led to extensive hydrothermal dolomitization and Sd precipitation.

The Qixia Formation cyclic layered facies-controlled dolomite reservoirs, the Lower Cambrian high-quality source rocks and caprocks, and the strike-slip faults as migration pathways, are conducive to oil and gas accumulation in the Qixia Formation dolomite. The central Sichuan Basin has a paleo-uplift background, which is favorable for the forming of a large gas region. Therefore, the facies-controlled porous dolomite reservoirs of the Qixia Formation in central Sichuan Basin are a key replacement option for the exploration of deep marine carbonate rocks.
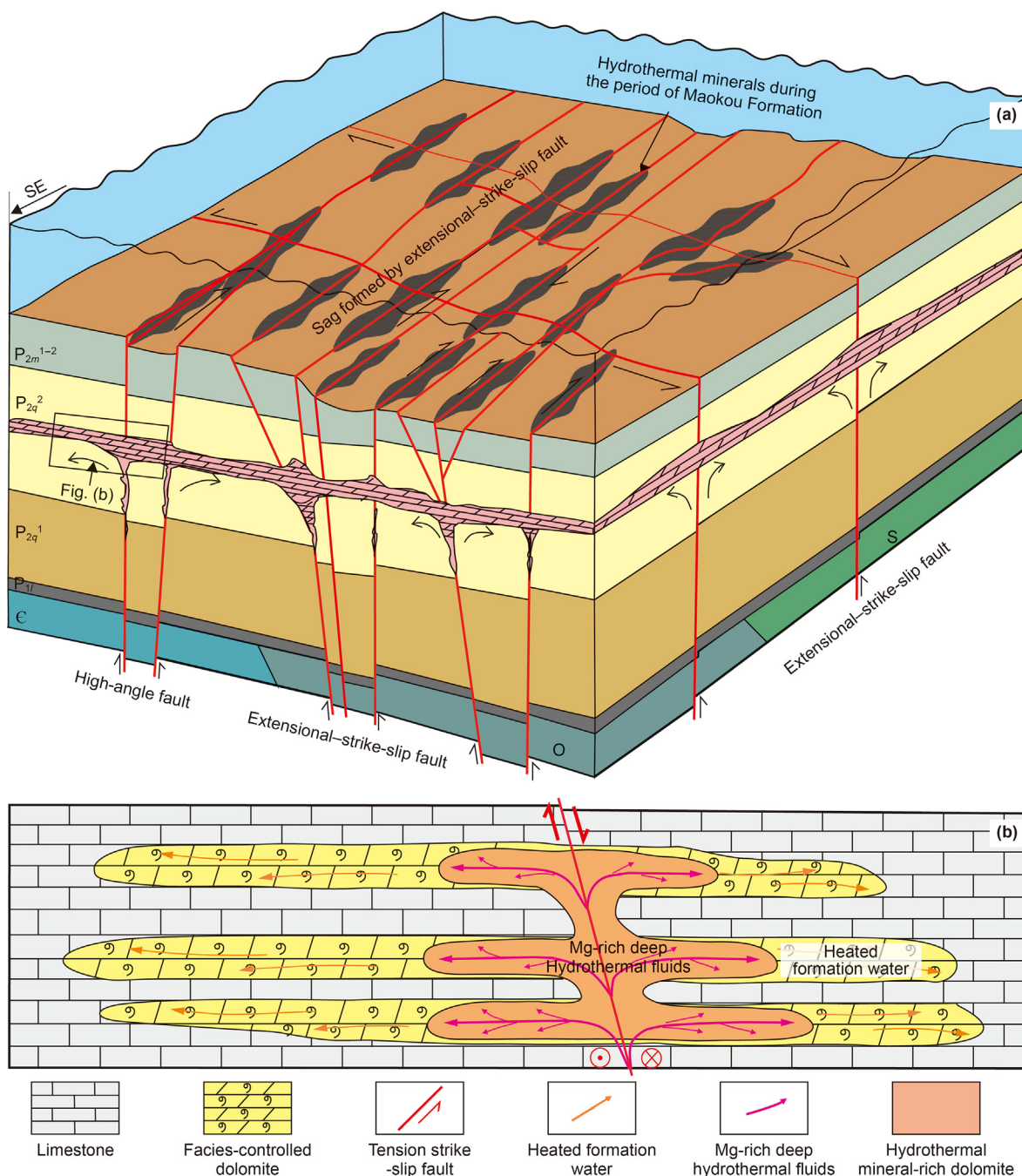
Fig. 17. (a) Genetic model of facies-controlled dolomite of the Qixia Formation in central Sichuan Basin; **(b)** Model of facies-controlled dolomite of the Qixia Formation in the box in (a).

CRediT authorship contribution statement

Xiao-Liang Bai: Writing − review & editing, Writing − original draft, Funding acquisition. **Long Wen:** Writing − review & editing, Writing − original draft. **Yong-Mei Zhang:** Writing − review & editing, Writing − original draft, Visualization, Software. **Xi-Hua Zhang:** Data curation, Conceptualization. **Jing Wang:** Methodology, Investigation. **Yan-Gui Chen:** Methodology, Investigation. **Si-Qiao Peng:** Software, Data curation. **Wei Wang:** Software, Investigation. **Jia-Yi Zhong:** Software, Resources. **Ya Li:** Visualization, Data curation. **Ping Gao:** Visualization, Validation.

Declaration of competing interest

The authors declare that they have no known competing financial interests or personal relationships that could have appeared to influence the work reported in this paper.

Acknowledgements

References

Adams, J.E., Rhodes, M.L., 1960. Dolomitization by seepage refluxion. AAPG (Am. Assoc. Pet. Geol.) Bull. 44 (12), 1912–1920. https://doi.org/10.1306/0BDA6263-16BD-11D7-8645000102C1865D.

Badiozamani, K., 1973. The dorag dolomitization model-application to the Middle Ordovician of Wisconsin. J. Sediment. Res. 43 (4), 965–984. https://doi.org/10.1306/74D728C9-2B21-11D7-8648000102C1865D.

Bau, M., Dulski, P., 1996. Distribution of yttrium and rare-earth elements in the penge and kuruman iron-formations, transvaal supergroup, South Africa. Precambrian Res. 79 (1–2), 37–55. https://doi.org/10.1016/0301-9268(95)00087-9.

Bau, M., Romer, R.L., Lüders, V., Dulski, P., 2003. Tracing element sources of hydrothermal mineral deposits: REE and Y distribution and Sr-Nd-Pb isotopes in fluorite from MVT deposits in the Pennine Orefield, England. Miner. Deposita 38 (8), 992–1008. https://doi.org/10.1007/s00126-003-0376-x.

Bodnar, R.J., 1993. Revised equation and table for determining the freezing point depression of H$_2$O-NaCl solutions. Geochem. Cosmochim. Acta 57 (3), 683–684. https://doi.org/10.1016/0016-7037(93)90378-A.

Chen, H.D., Hou, M.C., Liu, W.J., Tian, J.C., 2004. Basin evolution and sequence stratigraphic framework of South of China during hercynian cycle to indo-Chinese epoch. J. Chengdu Univ. Technol. (Sci. Technol. Ed.) 31 (6), 629–635. https://doi.org/10.3969/j.issn.1671-9727.2004.06.012 (in Chinese).

Chen, H.D., Qin, J.X., Wang, C.S., Shou, J.F., Li, X.H., 1999. Sequence-based lithofacies and paleogeographic characteristics and evolution of permian in South China. Acta Sedimentol. Sin. 17 (4), 510–521. https://doi.org/10.14027/j.cnki.cjxb.1999.04.002 (in Chinese).

Chen, H.D., Zhang, C.G., Huang, F.X., Hou, M.C., 2011. Filling process and evolutionary model of sedimentary sequence of middle-upper Yangtze craton in hercynian-indosinian (devonian- middle triassic). Acta Petrol. Sin. 27 (8), 2281–2298. CNKI:SUN:YSXB.0.2011-08-007 (in Chinese).

Chen, M.Q., 1989. A discussion of the origin of yangxin dolomite of lower permian in southwest Sichuan. Acta Sendimentologica Sinica 7 (2), 45–50. https://doi.org/10.14027/j.cnki.cjxb.1989.02.008 (in Chinese).

Chen, X., Zhao, W.Z., Zhang, L.P., Zhao, Z.J., Liu, Y.H., Zhang, B.M., Yang, Y., 2012. Discovery and exploration significance of structure- controlled hydrothermal dolomites in the Middle Permian of the central Sichuan Basin. Acta Pet. Sin. 33 (4), 562–569. https://doi.org/10.7623/syxb201204004 (in Chinese).

Consonni, A., Frixa, A., Maragliulo, C., 2018. Hydrothermal dolomitization: simulation by reaction transport modeling. Geological Society London Special Publications 435 (1), 235–244. https://doi.org/10.1144/SP435.13.

Davies, J.-G.R., Smith, L.B., 2006. Structurally controlled hydrothermal dolomite reservoir facies: an overview. AAPG (Am. Assoc. Pet. Geol.) Bull. 90 (11), 1641–1690. https://doi.org/10.1306/04290707031.

Duan, J.M., Zheng, J.F., Shen, A.J., Zhu, M., Yao, Q.Y., Hao, Y., 2021. Characteristics and genesis of dolomite reservoir of the lower permian Qixia Formation in central Sichuan Basin. Marine Origin Petroleum Geology 26 (4), 345–356. https://doi.org/10.3969/j.issn.1672-9854.2021.04.007 (in Chinese).

Fanning, K.A., Byrne, R.H., Breland, J.A., Betzer, P.R., Moore, W.S., Elsinger, R.J., Pyle, T.E., 1981. Geothermal springs of the West Florida continental shelf: evidence for dolomitization and radionuclide enrichment. Earth Planet Sci. Lett. 52 (2), 345–354. https://doi.org/10.1016/0012-821X(81)90188-6.

Guo, C., Chen, D.Z., Qing, H.R., Dong, S.F., Li, G.R., Wang, D., Qian, Y.X., Liu, C.G., 2016. Multiple dolomitization and later hydrothermal alteration on the Upper Cambrian-Lower Ordovician carbonates in the northern Tarim Basin, China. Mar. Petrol. Geol. 72, 295–316. https://doi.org/10.1016/j.marpetgeo.2016.01.023.

He, D.F., Li, D.S., Zhang, G.W., Zhao, L.Z., Fan, C., Lu, R.Q., Wen, Z., 2011. Formation and evolution of multi-cycle superposed Sichuan Basin, China. Chinese Journal of Geology 46 (3), 589–606. https://doi.org/10.3969/j.issn.0563-5020.2011.03.001 (in Chinese).

He, W.Y., Meng, Q.A., Yin, C.H., Wang, X.D., Zhang, H.J., Shi, J.B., 2022. Geological characteristics and favorable exploration plays of gas in Qixia Formation dolomite in Hechuan-Tongnan area of Sichuan Basin. Pet. Geol. Oilfield Dev. Daqing 41 (4), 1–11. https://doi.org/10.19597/J.ISSN.1000-3754.202104058 (in Chinese).

Hill, C.A., Polyak, V.J., Asmerom, Y., Provencio, P.P., 2016. Constraints on a Late Cretaceous uplift, denudation, and incision of the Grand Canyon region, southwestern Colorado Plateau, USA, from U-Pb dating of lacustrine limestone. Tectonics 35, 896–906. https://doi.org/10.1002/2016TC004166.

Hirani, J., Bastesen, E., Boyce, A., Corlett, H., Gawthorpe, R., Holli, C., John, C.M., Robertson, H., Rotevatn, A., Whitaker, F., 2018. Controls on the formation of stratabound dolostone bodies, hammam faraun fault block, gulf of suez. Sedimentology 65 (6), 1973–2002. https://doi.org/10.1111/sed.12454.

Hollis, C., Bastesen, E., Boyce, A., Corlett, H., Gawthorpe, R., Hirani, J., Rotevatn, A., Whitaker, F., 2017. Fault-controlled dolomitization in a rift basin. The Geological Society of America 45 (3), 219–222. https://doi.org/10.1130/G38s394.1.

Hsu, K.J., Siegenth, C., 1969. Preliminary experiments on hydrodynamic movement induced by evaporation and their bearing on the dolomite problem. Sedimentology 12 (1–2), 11–25. https://doi.org/10.1111/j.1365-3091.1969.tb00161.x.

Hu, G.C., Xie, Y.X., 1997. Carboniferous Gas Field in High Steep Structure of Eastern Sichuan, China. Beijing: Petroleum industry press, pp. 14–16 (in Chinese).

Huang, S.J., Lan, Y.F., Huang, K.K., Lv, J., 2014. Vug fillings and records of hydrothermal activity in the middle Permian Qixia Formation, western Sichuan Basin. Acta Petrol. Sin. 30 (3), 687–698. https://doi.org/10.0000/9c0d214e170b4-b44aeea4487a2c0ccfb (in Chinese).

Huang, S.J., Li, X.N., Huang, K.K., Lan, Y.F., Lv, J., Wang, C.M., 2012. Authigenic Noncarbonate minerals in hydrothermal dolomite of middle Permian Qixia Formation in the west of Sichuan Basin, China. J. Chengdu Univ. Technol. (Sci. Technol. Ed.) 39 (4), 343–352. https://doi.org/10.3969/j.issn.1671-9727.2012.04.001 (in Chinese).

Illing, L.V., Wells, A.J., 1965. Penecontemporary dolomite in the Persian Gulf: abstract. AAPG (Am. Assoc. Pet. Geol.) Bull. 48 (4), 532–533. https://doi.org/10.1306/BC743C93-16BE-11D7-8645000102C1865D.

Jiang, L., Cai, C.F., Worden, R.H., Crowley, S.F., Jia, L.Q., Zhang, K., Duncan, I.J., 2016. Multiphase dolomitization of deeply buried Cambrian petroleum reservoirs, Tarim Basin, north-west China. Sedimentology 63 (7), 2130–2157. https://doi.org/10.1111/sed.12300.

Jiang, L., Worden, R.H., Cai, C.F., Li, K.K., Xiang, L., Cai, L.L., He, X.Y., 2014. Dolomitization of gas reservoirs: the upper Permian changxing and lower triassic feixianguan formations, northeast Sichuan Basin, China. J. Sediment. Res. 84 (10), 792–815. https://doi.org/10.2110/jsr.2014.65.

Jiang, L., Shen, A.J., Wang, Z.C., Hu, A.P., Wang, Y.S., Luo, X.Y., Liang, F., Azmy, K., Pan, L.Y., 2022. U-Pb geochronology and clumped isotope thermometry of Neoproterozoic dolomites from China. Sedimentology 69 (7), 2925–2945. https://doi.org/10.1111/sed.13026.

Jiang, Z.B., Wang, X.Z., Zeng, D.M., Lu, T.M., Wang, B.Q., Zhang, J.Y., 2009. Constructive diagenesis and porosity evolution in the lower permian Qixia Formation of northwest sichuan. Chin. Geol. 36 (1), 101–109. https://doi.org/10.3969/j.issn.1000-3657.2009.01.008 (in Chinese).

Jin, Z.K., Feng, Z.Z., 1999. Origin of the lower permian in east yunnan-west sichuan dolomitization through leaching of basalts. Acta Sendimentologica Sinica 17 (3), 383–389. https://doi.org/10.3969/j.issn.1000-0550.1999.03.008 (in Chinese).

Jones, G.D., Smart, P.L., Whitaker, F.F., Rostron, B.J., Machel, H.G., 2003. Numerical modeling of reflux dolomitization in the Grosmont platform complex (Upper Devonian), Western Canada sedimentary basin. AAPG Bull. 87 (8), 1273–1298. https://doi.org/10.1306/03260302007.

Koeshidayatullah, A., Corlett, H., Stacey, J., Swart, P.K., Boyce, A., Robertson, H., Whitaker, F., Hollis, C., 2020. Evaluating new fault-controlled hydrothermal dolomitization models: insights from the cambrian dolomite, western Canadian sedimentary basin. Sedimentology 67 (6), 2945–2973. https://doi.org/10.1111/sed.12729.

Land, L.S., 1985. The origin of massive dolomite. J. Geol. Educ. 33 (2), 112–125. https://doi.org/10.5408/0022-1368-33.2.112.

Land, L.S., 1983. The application of stable isotopes to studies of the origin of dolomite and to problems of diagenesis of clastic sediments. In: Arthur, M.A., Anderson, T.F., Kaplan, I.R., Veizer, J., Land, L.S. (Eds.), Stable Isotopes in the Sedimentary Geology, vol. 10. SEPM Short Course Notes, pp. 411–422. https://doi.org/10.2110/scn.83.01.0000.

Lawrence, M.G., Greig, A., Collerson, K.D., Kamber, B.S., 2006. Rare earth element and yttrium variability in South east queensland waterways. Aquat. Geochem. 12 (1), 39–72. https://doi.org/10.1007/s10498-005-4471-8.

Li, F., Webb, G.E., Algeo, T.J., Kershaw, S., Lu, C.J., Oehlert, A.M., Gong, Q.L., Pourmand, A., Tan, X.C., 2019. Modern carbonate ooids preserve ambient aqueous REE signatures. Chem. Geol. 509, 163–177. https://doi.org/10.1016/j.chemgeo.2019.01.015.

Li, M.L., Tan, X.C., Su, C.P., Lu, F.F., Zhang, B.J., Pan, Z.Y., Xiao, D., 2020. Characteristics and genesis of sucrosic dolomite in middle permian chihsia formation, northwest Sichuan Basin: a case study from shangsi section. Geology Review 66 (3), 591–610. https://doi.org/10.16509/j.georeview.2020.03.005 (in Chinese).

Li, W., Yi, H.Y., Hu, W.S., Yang, G., Xiong, X., 2014. Tectonic evolution of caledonian paleohigh in the Sichuan Basin and its relationship with hydrocarbon accumulation. Nat. Gas. Ind. B 1 (1), 58–65. https://doi.org/10.3787/j.issn.1000-0976.2014.03.002.

Li, X.N., Huang, S.J., Huang, S.G., Huang, K.K., Yuan, T., Luo, W., 2016. Petrologic and geochemical characteristics and the origin of dolomites in the Qixia Formation in nanjiang county of the Sichuan Basin. Petroleum Geology & Experiment 38 (2), 251–258+265. https://doi.org/10.11781/sysydz201602251 (in Chinese).

Lu, F.F., Tan, X.C., Zhong, Y., Luo, B., Zhang, B.J., Zhang, Y., Li, M.L., Xiao, D., Wang, X.F., Zeng, W., 2020. Origin of the penecontemporaneous sucrosic dolomite in the permian Qixia Formation, northwestern Sichuan Basin, SW China. Petrol. Explor. Dev. 47 (6), 1218–1234. https://doi.org/10.1016/S1876-3804(20)60131-3.

Lu, X.S., Gui, L.L., Wang, Z.C., Liu, S.B., Liu, Q., Fan, J.J., Chen, W.Y., Ma, X.Z., Jiang, H., Fu, X.D., Li, W.Z., Zhong, Y., Li, K.Y., Xie, W.R., 2024. Activity time of strike-slip faults and their controlling effects on hydrocarbon accumulation in central Sichuan Basin: evidence from U-Pb dating and fluid inclusions of cements in fault zone. ACTA PETROLEI SINICA 45 (4), 642–658. https://doi.org/10.7623/syxb202404003 (in chinese).

Machel, H.G., 2004. Concepts and models of dolomitization: a critical reappraisal. Geological Society of London Special Publications 235 (1), 7–63. https://doi.org/10.1144/GSL.SP.2004.235.01.02.

Machel, H.G., Anderson, J.H., 1989. Pervasive subsurface dolomitization of the Nisku Formation in central Alberta. J. Sediment. Res. 59 (6), 891–911. https://doi.org/10.1306/212F90AC-2B24-11D7-8648000102C1865D.

Major, R.P., Lloyd, R.M., Lucia, F.J., 1992. Oxygen isotope composition of Holocene dolomite formed in a humid hypersaline setting. Geology 20 (7), 586–588. https://doi.org/10.1130/0091-7613(1992)020<0586:OICOHD>2.3.CO;2.

McLennan, S.M., 1989. Rare earth elements in sedimentary rocks: influence of provenance and sedimentary processes. Rev. Mineral. Geochem. 21 (1), 170–200. https://doi.org/10.1515/9781501509032-010.

Pan, L.Y., Hu, A.P., Liang, F., Jiang, L., Hao, Y., Feng, Y.X., Shen, A.J., Zhao, J.X., 2021.

Diagenetic conditions and geodynamic setting of the middle Permian hydro-thermal dolomites from southwest Sichuan Basin, SW China: Insights from in situ U–Pb carbonate geochronology and isotope geochemistry. Mar. Petrol. Geol. 129, 105080. https://doi.org/10.1016/j.marpetgeo.2021.105080.

Pan, L.Y., Shen, A.J., Zhao, J.X., Hu, A.P., Hao, Y., Liang, F., Feng, Y.X., Wang, X.F., Jiang, L., 2020. LA-ICP-MS U-Pb geochronology and clumped isotope constraints on the formation and evolution of an ancient dolomite reservoir: the Middle Permian of northwest Sichuan Basin (SW China). Sediment. Geol. 407, 105728. https://doi.org/10.1016/j.sedgeo.2020.105728.

Shi, G.R., 2001. Possible influence of Gondwana glaciation on low-latitude carbonate sedimentation and trans-equatorial faunal migration: the Lower Permian of South China. J. Geosci. 5 (1), 57–63. https://doi.org/10.1007/BF02910173.

Shi, G.R., Grunt, T.A., 2000. Permian Gondwana-Boreal antitropicality with special reference to brachiopod faunas. Palaeogeogr. Palaeoclimatol. Palaeoecol. 155 (3), 239–263. https://doi.org/10.1016/S0031-0182(99)00118-2.

Shields, M.J., Brady, P.V., 1995. Mass balance and fluid flow constraints on regional-scale dolomitization, Late Devonian, Western Canada Sedimentary Basin. Bull. Can. Petrol. Geol. 43 (4), 371–392. https://doi.org/10.35767/gscpgbull.44.3.572.

Song, J.M., Liu, S.G., Jin, X., Wang, H., Fan, J.P., Jiang, Q.C., Tian, X.B., Ye, Y.H., Li, Y., Li, Z.W., Yang, D., Wang, J.R., Luo, P., 2022. A new model of source-reservoir association and new fields of oil and gas exploration in the Middle Permian sepiolite bearing strata, Sichuan Basin, China. Journal of Chengdu University of Technology (Science & Technology Edition 49 (2), 129–149. https://doi.org/10.3969/j.issn.1671-9727.2022.02.01 (in Chinese).

Tostevin, R., Shields, G.A., Tarbuck, G.M., et al., 2016. Effective use of cerium anomalies as a redox proxy in carbonate-dominated marine settings. Chem. Geol. 438, 146–162. https://doi.org/10.1016/j.chemgeo.2016.06.027.

Vasconcelos, C., Mckenzie, J.A., 1997. Microbial mediation of modern dolomite precipitation and diagenesis under anoxic conditions (Lagoa Vermelha, Rio de Janeiro, Brazil). J. Sediment. Res. 67 (3), 378–390. https://doi.org/10.1306/D4268577-2B26-11D7-8648000102C1865D.

Veizer, J., Ala, D., Azmy, K., Bruckschen, P., Buhl, D., Bruhn, F., Carden, G.A.F., Diener, A., Ebneth, S., Godderis, Y., Jasper, T., Korte, C., Pawellek, F., Podlaha, O.G., Strauss, H., 1999. $^{87}Sr/^{86}Sr$, $\delta^{13}C$ and $\delta^{18}O$ evolution of Phanerozoic seawater. Chem. Geol. 161 (1–3), 58–88. https://doi.org/10.1016/S0009-2541(99)00081-9.

Wang, H., Shen, H., Huang, D., Shi, X.W., Li, Y., Yuan, X.L., Yang, Y.R., 2014. Origin and distribution of hydrothermal dolomites of the middle Permian in the Sichuan Basin. Nat. Gas. Ind. 34 (9), 25–32. https://doi.org/10.3787/j.issn.1000-0976.2014.09.004 (in Chinese).

Wang, J.B., He, Z.L., Zhu, D.Y., Liu, Q.Y., Ding, Q., Li, S.J., Zhang, D.W., 2020. Petro-logical and geochemical characteristics of the botryoidal dolomite of deying Formation in the Yangzi craton, South China: constraints on terminal Edicaran "dolomite seas." Sediment. Geol. 406, 105722. https://doi.org/10.1016/j.sedgeo.2020.105722.

Warren, J., 2000. Dolomite: occurrence, evolution and economically important as-sociations. Earth Sci. Rev. 52 (1–3), 1–81. https://doi.org/10.1016/S0012-8252(00)00022-2m.

Wen, L., Wang, H., Xu, L., Zhang, Y., Yuan, H.F., Chen, S.L., Qiao, Y.P., Shen, C., 2021. Characteristics and main controlling factors of gas accumulation of the middle Permian Qixia Formation in western Sichuan Basin. China Petroleum Explora-tion 26 (6), 68–81. https://doi.org/10.3969/j.issn.1672-7703.2021.06.005 (in Chinese).

Woodhead, J.D., Hergt, J.M., 2001. Strontium, neodymium and lead isotope analyses of NIST glass certified reference materials: SRM 610, 612, 614. Geostandards Newsletter 25 (2–3), 261–266. https://doi.org/10.1111/j.1751-908x.2001.tb00601.x.

Xu, H.L., Wei, G.Q., Jia, C.Z., Yang, W., Zhou, T.W., Xie, W.R., Li, C.X., Luo, B.W., 2012. Tectonic evolution of the Leshan-Longnüsi paleo-uplift and its control on gas accumulation in the Sinian strata, Sichuan Basin. Petrol. Explor. Dev. 39 (4), 406–416. https://doi.org/10.1016/S1876-3804(12)60060-3 (in Chinese).

Yin, H.F., Yu, J.X., Luo, G.M., Song, H.J., Xu, Z., 2018. Biotic influence on the formation of Icehouse Climates in geologic history. Geoscience 43 (11), 3809–3822. https://doi.org/10.3799/dqkx.2018.117 (in Chinese).

Yin, J.F., Gu, Z.D., Li, Q.F., 2013. Characteristics of deep-rooted faults and their geological significances in Dachuanzhong area, Sichuan Basin. Oil Gas Geol. 34 (3), 376–382. https://doi.org/10.11743/ogg20130314 (in Chinese).

Zenger, D.H., 1983. Burial dolomitization in the Lost Burro Formation (Devonian), east-central California, and the significance of late diagenetic dolomitization. Geology 11 (9), 519–522. https://doi.org/10.1130/0091-7613(1983)11<519:BDITLB>2.0.CO;2.